



HAL
open science

What was the Paleogene latitude of the Lhasa terrane? A reassessment of the geochronology and paleomagnetism of Linzizong volcanic rocks (Linzhou Basin, Tibet)

Wentao Huang, Guillaume Dupont-Nivet, Peter C. Lippert, Douwe J.J. van Hinsbergen, Mark J. Dekkers, Ross Waldrip, Morgan Ganerod, Xiaochun Liu, Zhaojie Guo, Paul Kapp

► To cite this version:

Wentao Huang, Guillaume Dupont-Nivet, Peter C. Lippert, Douwe J.J. van Hinsbergen, Mark J. Dekkers, et al.. What was the Paleogene latitude of the Lhasa terrane? A reassessment of the geochronology and paleomagnetism of Linzizong volcanic rocks (Linzhou Basin, Tibet). *Tectonics*, 2015, 34 (3), pp.594-622 10.1002/2014TC003787 . insu-01120570

HAL Id: insu-01120570

<https://insu.hal.science/insu-01120570>

Submitted on 29 Jun 2016

HAL is a multi-disciplinary open access archive for the deposit and dissemination of scientific research documents, whether they are published or not. The documents may come from teaching and research institutions in France or abroad, or from public or private research centers.

L'archive ouverte pluridisciplinaire **HAL**, est destinée au dépôt et à la diffusion de documents scientifiques de niveau recherche, publiés ou non, émanant des établissements d'enseignement et de recherche français ou étrangers, des laboratoires publics ou privés.

RESEARCH ARTICLE

10.1002/2014TC003787

Key Points:

- Lower Linzizong Group volcanic rocks were hydrothermally chemically remagnetized
- Upper Linzizong Group volcanic rocks retain a primary remanence
- The Paleogene latitude of the Lhasa terrane was $20 \pm 4^\circ\text{N}$

Supporting Information:

- Supplement A, Supplement B, and Tables S1–S8

Correspondence to:

W. Huang,
W.Huang@uu.nl

Citation:

Huang, W., G. Dupont-Nivet, P. C. Lippert, D. J. J. van Hinsbergen, M. J. Dekkers, R. Waldrip, M. Ganerød, X. Li, Z. Guo, and P. Kapp (2015), What was the Paleogene latitude of the Lhasa terrane? A reassessment of the geochronology and paleomagnetism of Linzizong volcanic rocks (Linzhou basin, Tibet), *Tectonics*, 34, 594–622, doi:10.1002/2014TC003787.

Received 19 NOV 2014

Accepted 19 FEB 2015

Accepted article online 22 FEB 2015

Published online 26 MAR 2015

What was the Paleogene latitude of the Lhasa terrane? A reassessment of the geochronology and paleomagnetism of Linzizong volcanic rocks (Linzhou basin, Tibet)

Wentao Huang^{1,2}, Guillaume Dupont-Nivet^{1,2,3,4}, Peter C. Lippert^{5,6}, Douwe J. J. van Hinsbergen², Mark J. Dekkers², Ross Waldrip⁵, Morgan Ganerød⁷, Xiaochun Li⁸, Zhaojie Guo¹, and Paul Kapp⁵

¹Key Laboratory of Orogenic Belts and Crustal Evolution, Ministry of Education, School of Earth and Space Sciences, Peking University, Beijing, China, ²Department of Earth Sciences, Utrecht University, Utrecht, Netherlands, ³Géosciences Rennes, UMR 6118, Université de Rennes 1, Rennes CEDEX, France, ⁴Institute of Earth and Environmental Science, University of Potsdam, Potsdam-Golm, Germany, ⁵Department of Geosciences, University of Arizona, Tucson, Arizona, USA, ⁶Department of Geology & Geophysics, University of Utah, Salt Lake City, Utah, USA, ⁷Geodynamikk, Geological Survey of Norway, Trondheim, Norway, ⁸Department of Earth Sciences, The University of Hong Kong, Hong Kong, China

Abstract The Paleogene latitude of the Lhasa terrane (southern Tibet) can constrain the age of the onset of the India-Asia collision. Estimates for this latitude, however, vary from 5°N to 30°N , and thus, here, we reassess the geochronology and paleomagnetism of Paleogene volcanic rocks from the Linzizong Group in the Linzhou basin. The lower and upper parts of the section previously yielded particularly conflicting ages and paleolatitudes. We report consistent $^{40}\text{Ar}/^{39}\text{Ar}$ and U-Pb zircon dates of ~ 52 Ma for the upper Linzizong, and $^{40}\text{Ar}/^{39}\text{Ar}$ dates (~ 51 Ma) from the lower Linzizong are significantly younger than U-Pb zircon dates (64–63 Ma), suggesting that the lower Linzizong was thermally and/or chemically reset. Paleomagnetic results from 24 sites in lower Linzizong confirm a low apparent paleolatitude of $\sim 5^\circ\text{N}$, compared to the upper part ($\sim 20^\circ\text{N}$) and to underlying Cretaceous strata ($\sim 20^\circ\text{N}$). Detailed rock magnetic analyses, end-member modeling of magnetic components, and petrography from the lower and upper Linzizong indicate widespread secondary hematite in the lower Linzizong, whereas hematite is rare in upper Linzizong. Volcanic rocks of the lower Linzizong have been hydrothermally chemically remagnetized, whereas the upper Linzizong retains a primary remanence. We suggest that remagnetization was induced by acquisition of chemical and thermoviscous remanent magnetizations such that the shallow inclinations are an artifact of a tilt correction applied to a secondary remanence in lower Linzizong. We estimate that the Paleogene latitude of Lhasa terrane was $20 \pm 4^\circ\text{N}$, consistent with previous results suggesting that India-Asia collision likely took place by ~ 52 Ma at $\sim 20^\circ\text{N}$.

1. Introduction

Establishing the paleolatitude histories of terranes within N-S closing oceanic basins is a common approach to date collisional events [e.g., *Gilder and Courtillot*, 1997], such as the one between Greater India and the Lhasa terrane that bordered the Cretaceous Neotethyan ocean. Paleomagnetic investigations of the paleolatitude of the Lhasa terrane, which formed the southern edge of the Asian continent since the Cretaceous, started in the 1980s and early 1990s [*Zhu et al.*, 1981; *Pozzi et al.*, 1982; *Westphal and Pozzi*, 1983; *Achache et al.*, 1984; *Lin and Watts*, 1988; *Chen et al.*, 1993]. Recently, several groups attempted to improve on these pioneering studies by generating larger datasets and using more sophisticated analytical procedures [*Chen et al.*, 2010; *Dupont-Nivet et al.*, 2010b; *Liebke et al.*, 2010; *Sun et al.*, 2010; *Tan et al.*, 2010; *Chen et al.*, 2012; *Liebke et al.*, 2012; *Sun et al.*, 2012; *van Hinsbergen et al.*, 2012; *Huang et al.*, 2013; *Chen et al.*, 2014; *Lippert et al.*, 2014; *Yang et al.*, 2014; *Huang et al.*, 2015b]. Most of the later studies focused on the regionally extensive Linzizong Group composed of ~ 69 –44 Ma lavas, ignimbrites, ash fall tuffs, and sedimentary rocks. Recent paleolatitude estimates for the Lhasa terrane derived from Linzizong Group rocks vary from 5°N to 30°N , however. This range of paleolatitudes, often from the same rock units, corresponds to a discrepancy of more than 2500 km for the position of the southern Asian margin, and as a consequence, the paleomagnetically inferred age of the collision between the leading edge of Greater India and the Lhasa terrane ranges from 35 to 65 Ma.

The Linzizong Group exposed in the Linzhou basin of southern Tibet (Figure 1) has been a primary target for paleolatitude studies because of its proximity to Lhasa and outstanding outcrop exposures. Highly contrasting paleomagnetic results from different intervals of the Linzizong Group near Linzhou have been reported by *Achache et al.* [1984], *Chen et al.* [2010], *Dupont-Nivet et al.* [2010b], *Liebke et al.* [2010], *Tan et al.* [2010], *Liebke et al.* [2012], *Huang et al.* [2013], and *Chen et al.* [2014]. The source of this disparity remains unclear, although our recent work on the Linzizong Group in the Linzhou basin suggests some potential explanations. We have shown that sedimentary rocks from the uppermost interval of the Linzizong Group (~52 Ma) have a strong bedding-parallel fabric and magnetic directional distribution that are consistent with sedimentary inclination shallowing [*Huang et al.*, 2013]. *Tan et al.* [2010] reported similar phenomena and biasing in Cretaceous sediments below the Linzizong Group in this basin. We also showed that undersampling secular variation in studies focused on the volcanic intervals is another strong bias in many of the published paleomagnetic poles from the Linzizong Group [*Lippert et al.*, 2014]. Large datasets from volcanic rocks [*Dupont-Nivet et al.*, 2010b; *van Hinsbergen et al.*, 2012; *Lippert et al.*, 2014], as well as inclination shallowing-corrected results from sedimentary rocks directly overlying these volcanic rocks [*Huang et al.*, 2013], provide a consistent Paleogene latitude estimate of $\sim 20 \pm 4^\circ\text{N}$.

Published paleomagnetic results from the lower Linzizong Group in the Linzhou basin, however, were interpreted to have been deposited at a much lower paleolatitude of $\sim 5^\circ\text{N}$ [*Chen et al.*, 2010, 2014]. Such a scenario requires a >1500 km northward shift of the Lhasa terrane within ~ 10 Myr relative to an essentially latitudinally stationary Eurasia. This paleogeography requires a remarkably fast northward motion of Tibetan lithosphere with a velocity of ~ 15 cm/yr, which is much higher than reconstructed Cenozoic intra-Asian shortening rates of ~ 1 – 1.5 cm/yr and which is almost equal to the India-Asia convergence rate in this time period [*van Hinsbergen et al.*, 2011a, 2011b]. Moreover, such a scenario also requires that the Lhasa terrane has moved >1000 km south relative to Eurasia (requiring major extension in Asia) between the Late Cretaceous and Paleocene [*Tan et al.*, 2010; *Chen et al.*, 2012; *Sun et al.*, 2012; *van Hinsbergen et al.*, 2012; *Chen et al.*, 2014; *Lippert et al.*, 2014; *Ma et al.*, 2014; *Yang et al.*, 2014]. These scenarios of rapid yo-yo-like plate tectonic motions of the Lhasa terrane are neither predicted by the apparent polar wander path of Eurasia since Cretaceous [*Torsvik et al.*, 2008, 2012; *Torsvik and Cocks*, 2013] nor supported by geological observations and reconstructions [*Dewey et al.*, 1989; *Yin and Harrison*, 2000; *Johnson*, 2002; *Replumaz and Tapponnier*, 2003; *van Hinsbergen et al.*, 2011b].

We recently reinvestigated a section of the lower Linzizong volcanic-bearing strata in the Nanmulin basin, 50 km northeast of Xigaze (Figure 1a), where some of these low paleolatitudes have been reported [*Chen et al.*, 2010]. Our rock magnetic analyses, negative fold tests, and petrographic observations demonstrate that these rocks do not retain their primary magnetization but are instead remagnetized to varying amounts. The failure to recognize this remagnetization leads to an interpreted paleolatitude of $\sim 7^\circ\text{N}$, instead of the correct paleolatitude of $\sim 20^\circ\text{N}$ [*Huang et al.*, 2015b]. The pervasive yet easily overlooked remagnetization of the Linzizong Group in the Nanmulin basin therefore demands a thorough rock magnetic reinvestigation of the Linzizong stratigraphy in the Linzhou basin to assess if the paleolatitude estimates, including our own, calculated from these rocks are also biased by remagnetization. In the Linzhou basin, however, the structure precludes a paleomagnetic fold test and reversed directions are too sparse for a statistically meaningful reversals test; therefore, we must thoroughly characterize the magnetic petrology and thermal histories of these units.

In this paper, we reevaluate the paleomagnetism of the lower Linzizong Group in the Linzhou basin using several approaches. (1) $^{40}\text{Ar}/^{39}\text{Ar}$ and U-Pb dates were obtained from the same samples collected throughout the entire volcanic succession for the first time. (2) We test whether the published shallow paleomagnetic directions from the lower Linzizong Group are reproducible. (3) We investigate the anisotropy of magnetic susceptibility of the lower Linzizong Group to compare with the upper intervals and to estimate the potential effect of magnetic fabrics on remanence directions [*Huang et al.*, 2013]. (4) We provide detailed rock magnetic analyses focusing on the lower Linzizong Group, utilizing thermomagnetic experiments, hysteresis measurements, first-order reversal curves (FORC) diagrams, and isothermal remanent magnetization (IRM) component analysis to evaluate the relative age and carriers of the remanent magnetization(s). Equivalent rock magnetic studies have been applied to the upper Linzizong Group [*Dupont-Nivet et al.*, 2010b; *Huang et al.*, 2013]. (5) To enable further comparison of volcanic rocks between the lower and upper Linzizong Group, we applied end-member modeling of the acquisition curve of IRM [*Gong et al.*, 2009b] to identify potential differences in mechanisms for remanence acquisition. (6) Finally, we use optical and scanning electron

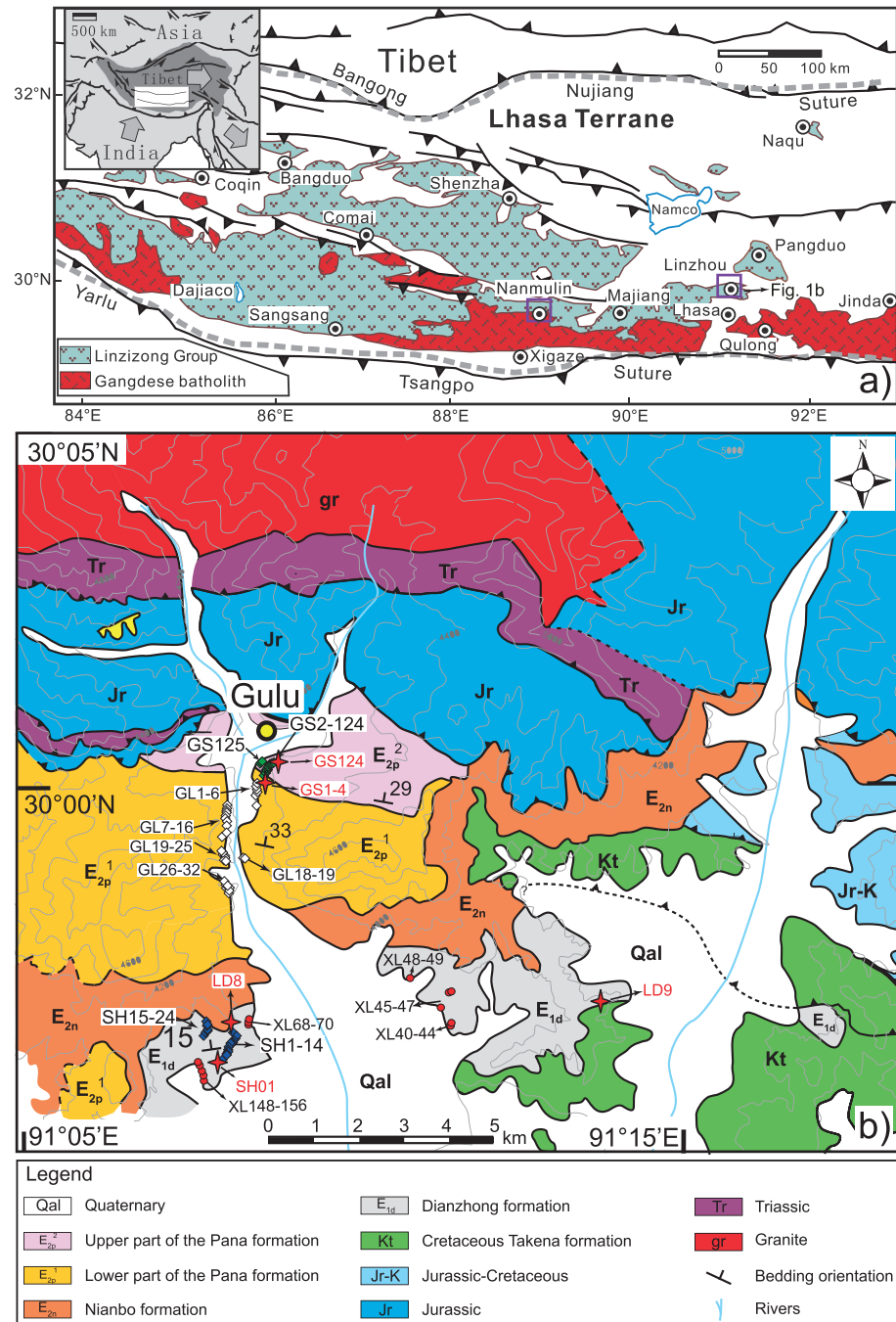


Figure 1. (a) Simplified geological map showing the distribution of the Gangdese batholith and associated Linzong volcanic successions in the Lhasa terrane, southern Tibet [modified from Yin and Harrison, 2000; Lee et al. 2009]; (b) simplified geologic map of the Linzhou basin [modified from He et al., 2007]. Diamonds and dots represent paleomagnetic sampling locations: white diamond—Dupont-Nivet et al. [2010b] from lower E_{2p}, green diamond—Huang et al. [2013] from upper E_{2p}, and blue diamond—this research from E_{1d}. Red dot: Chen et al. [2010] and Chen et al. [2014] from E_{1d}. Red stars represent geochronological sampling locations.

microscopy (SEM) to visually characterize the rock magnetic minerals and their relative ages of formation, and to verify rock magnetic results.

We use the described observations to propose possible mechanisms and ages of the remanence acquisition for the lower and upper volcanic rocks in the Linzhou basin and to reevaluate the reliability of published

paleomagnetic results. We also discuss potential pitfalls in determining a reliable paleolatitude from cryptically remagnetized lavas. Finally, we provide an assessment of the most reliable estimates for the Paleogene latitude of the Lhasa terrane.

2. Geologic Background

The Lhasa terrane was the southernmost margin of continental Eurasia, separated from Greater India by the Neotethyan ocean prior to the India-Asia collision that began during the early Paleogene [Tapponnier *et al.*, 1981; Burg *et al.*, 1983; Allegre *et al.*, 1984; Burg and Chen, 1984; Sengor, 1984; Dewey *et al.*, 1988; Yin and Harrison, 2000]. To the south, it is separated from the Tibetan Himalaya and India affinity rocks by the Yarlung-Tsangpo suture zone. To the north, it is separated from the Qiangtang continental block by the Late Jurassic-Cretaceous Bangong-Nujiang suture zone in central Tibet (Figure 1a) [Dewey *et al.*, 1988; Yin and Harrison, 2000; Kapp *et al.*, 2007a]. Northward subduction of the Neotethyan oceanic lithosphere beneath Eurasia produced a Cordilleran-type continental margin, manifested by the Gangdese batholith and associated Linzizong Group volcanic rocks along the southern margin of the Lhasa terrane [Coulon *et al.*, 1986; Yuquans, 1995; Ding *et al.*, 2003; Lee *et al.*, 2009; Jiang *et al.*, 2014; Pan *et al.*, 2014]. The Linzizong Group volcanic rocks are widely distributed in an east-west trending elongated belt along the northern edge of the Gangdese batholith (Figure 1a). The Linzizong Group erupted from ~69 to ~41 Ma determined by $^{40}\text{Ar}/^{39}\text{Ar}$ and U-Pb dates [Coulon *et al.*, 1986; Zhou *et al.*, 2004; Wu *et al.*, 2005; He *et al.*, 2007; Lee *et al.*, 2009; Chen *et al.*, 2014; Ding *et al.*, 2014]. This eruptive interval spans the India-Asia collision age of ~58–50 Ma inferred from stratigraphic and metamorphic studies [Garzanti *et al.*, 1987; de Sigoyer *et al.*, 2000; Leech *et al.*, 2005; Green *et al.*, 2008; Guillot *et al.*, 2008; Najman *et al.*, 2010; Hu *et al.*, 2012; DeCelles *et al.*, 2014; Orme *et al.*, 2014]. Thus, the Linzizong Group provides an ideal target for paleomagnetic investigations of the latitude history of the Lhasa terrane before and during the collision between the Tibetan Himalaya and the Lhasa block.

The Linzizong Group unconformably overlies strongly deformed Mesozoic strata. It is particularly well exposed and studied in the Linzhou basin, where it has a total thickness of ~3500 m and is divided into three formations, which are from bottom to top: the Dianzhong Formation (E_{1d}), the Nianbo Formation (E_{2n}), and the Pana Formation (E_{2p}) (Figure 1b) [Burg *et al.*, 1983; Xu *et al.*, 1985; Coulon *et al.*, 1986; Team of Regional Geological Survey of the Bureau of Geology and Mineral Resources of Tibet Autonomous Region, 1990; Liu, 1993; Mo *et al.*, 2003; He *et al.*, 2007; Leier *et al.*, 2007; Mo *et al.*, 2007]. E_{1d} strata lie unconformably on the Cretaceous Takena Formation. They are composed of andesitic lavas, dacitic to rhyolitic ash-tuff layers, and ignimbrite/pyroclastic flows (Figures 2a–2i). A gently dipping angular unconformity separates E_{1d} from E_{2n} , with bedding of E_{2n} ~5° steeper than that of E_{1d} (Figures 2j and 2k). The lower E_{2n} consists of two main repeated sequences of mudstone, conglomerate, and limestone layers at the bottom (Figure 2l). The top of E_{2n} contains tuffs and thin-layered calcareous mudstone intercalated with thick ash deposits. E_{2p} overlies E_{2n} with a slightly angular unconformity and is dominated by brown-gray dacitic lapilli tuffs with lapilli in the lower part (E_{2p}^1 in Figure 1b) and interbedded sandstone, siltstone, mudstone, and ash/tuff deposits in the upper part (E_{2p}^2 in Figure 1b). Basic dyke swarms dated to ~52 Ma are prevalent in the underlying Cretaceous Takena Formation, E_{1d} , and E_{2n} (Figures 2h, 2j, and 2k) [Yue and Ding, 2006; He *et al.*, 2007].

Several radiometric studies from the Linzhou basin, based primarily on U-Pb and $^{40}\text{Ar}/^{39}\text{Ar}$ techniques, have yielded volcanic emplacement ages from 69 to 44 Ma [BGMRXAR, 1993; Mo *et al.*, 2003; Zhou *et al.*, 2004; He *et al.*, 2007; Lee *et al.*, 2007; Ding *et al.*, 2014]. U-Pb zircon results are generally more concordant and show less within-site scatter than whole rock $^{40}\text{Ar}/^{39}\text{Ar}$ ages. This discrepancy may be attributed to the thermal history of the Linzhou basin [He *et al.*, 2007], which we will discuss below. $^{40}\text{Ar}/^{39}\text{Ar}$ dating of the dykes in E_{1d} and E_{2n} has yielded a plateau age of 52.9 ± 0.4 Ma [Yue and Ding, 2006], which is consistent with the zircon U-Pb ages of the dykes intruding in the Takena Formation [He *et al.*, 2007].

3. Paleomagnetic and Geochronologic Sampling

We have focused on volcanic rocks from E_{1d} and E_{2p} primarily because previous results from these units have yielded >15° discrepancies in the Paleogene latitude history for the southern Lhasa terrane [Achache *et al.*, 1984; Chen *et al.*, 2010; Dupont-Nivet *et al.*, 2010b; Liebke *et al.*, 2010; Tan *et al.*, 2010]. To supplement

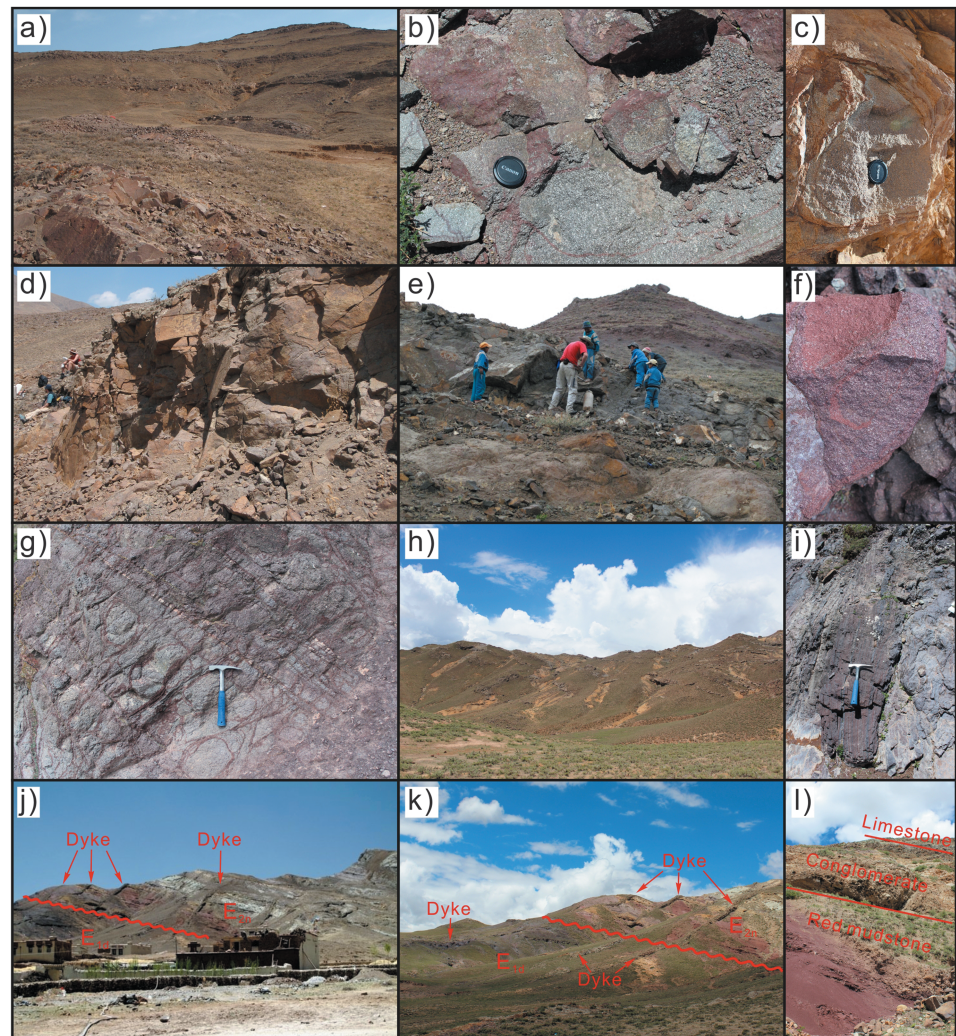


Figure 2. Field observations of the lower part of the Linzizong Group in the Linzhou basin. (a and b) Lava flows at the bottom of E_{1d} are fresh with minor surficial alteration or alteration along cracks. (c and d) Lava flows in the middle part of the sampled E_{1d} are altered to yellow-red. (e) Sampled lava flows from E_{1d} ; note the up-section change in color from blue-gray to red. (f) All lava flows in the upper part of E_{1d} are red colored. (g) Alteration of the lava flows close to dykes is characterized by precipitation of secondary hematite in microfractures. (h) E_{1d} is pervasively intruded by dykes. (i) Strongly jointed lava flows from the top of E_{1d} . (j and k) Dykes cut across the unconformity between E_{1d} and E_{2n} . (l) Strata of E_{2n} above the unconformity are composed of red mudstone, conglomerate, and limestone.

the 281 characteristic remanent magnetization (ChRM) directions presented in Dupont-Nivet *et al.* [2010b] and Huang *et al.* [2013] from E_{2p} volcanic rocks, we collected 24 volcanic sites within volcanic horizons (192 oriented cores, SH01 through SH24, site code increases up-section) of E_{1d} (Figure 1b). Standard 2.5 cm diameter paleomagnetic cores were collected using a portable gasoline-powered drill and oriented with magnetic and sun compasses (average absolute difference between magnetic and sun compass readings is 0° at all localities). Each paleomagnetic sampling site consisted of eight independent cores collected across the thickness of the lavas and across 2–4 m of lateral outcrop. Bedding attitudes determined by planar orientations of the top surface of the volcanic beds were measured throughout the section at several sampling sites. For the lower part of E_{1d} (SH01–SH13), a mean bedding orientation (dip azimuth = 9.2°N , dip = 16.6° ; $a_{95} = 4.2^\circ$) from 10 measurement sites was applied to correct the samples for bedding tilt (Table S1 in the supporting information). For the upper part of E_{1d} (SH14–SH24), nine measurement sites (Table S1) yielded a different mean bedding orientation (dip azimuth = 339°N , dip = 15.2° ; $a_{95} = 3.8^\circ$).

To detect potential thermal disturbance and to constrain the relative ages of remanence acquisition through the entire succession, samples for geochronologic studies were collected from E_{1d} (at the paleomagnetic sampling locations of site SH01) and from the tuff layers of E_{2p} (paleomagnetic sites GS1–4 and GS124) (Figure 1b). Another sample (LD8) was collected from the lava flow near the top of E_{1d} and a few hundred meters from the sampled section (Figure 1b). One additional sample (LD9) was collected from a dyke intruding the Cretaceous redbeds and E_{1d} to the east of the paleomagnetic sampling locations (Figure 1b); these dykes are described by *Liebke et al.* [2010] and *Liebke et al.* [2012].

4. Geochronology

Both $^{40}\text{Ar}/^{39}\text{Ar}$ whole rock and U-Pb zircon geochronology were conducted on GS1–4, GS124, and SH01. Samples LD8 and LD9 were dated only using U-Pb zircon geochronology. Methods and procedures for $^{40}\text{Ar}/^{39}\text{Ar}$ whole rock geochronology and U-Pb zircon geochronology are described in supporting information. The analytical data are reported in Tables S2 and S3.

4.1. $^{40}\text{Ar}/^{39}\text{Ar}$ Whole Rock Geochronology

The apparent age spectra and inverse isochron age results are displayed in Figures 3a–3c, and the results are listed in Table S2. Most samples show varying degrees of disturbance with high scatter [mean square weighted deviation (MSWD) \gg critical values; Figures 3a–3c] so that only one true weighted mean plateau age could be calculated (Figures 3a–3c). The remaining ages are reported by their weighted means from the spectrum analysis [*Renne et al.*, 1998]. The number of steps selected in the age calculations does not change the reported ages significantly. Due to the high scatter, caution must be taken when interpreting the ages; however, we may use them for comparative purposes, for example, between individual samples, as well as between geochronologic methods (i.e., Ar-Ar and U-Pb).

Samples GS1–4 and GS124 from E_{2p} yield dates of 50.1 ± 1.2 and 50.2 ± 1.0 Ma (Figures 3a and 3b), respectively; these dates overlap with each other at the 95% confidence level. Sample SH01 from the older E_{1d} strata yields a similar age of 51.3 ± 0.9 Ma (Figure 3c).

4.2. U-Pb Zircon Geochronology

Zircons from samples GS1–4 and GS124 are euhedral and show clear oscillatory zoning with rare inherited cores. For samples GS1–4, 13 spot analyses of 13 individual zircon grains provide a weighted mean age of 52.5 ± 1.2 Ma (2σ , MSWD = 0.2), with individual zircon ages that range between 50.2 and 54.6 Ma (Figure 3a). The ages are all concordant. For sample GS124, 21 spot analyses of 21 individual zircon grains provide a weighted mean age of 52.0 ± 0.7 Ma (2σ , MSWD = 0.6), with individual zircon ages that range between 50.6 and 54.4 Ma (Figure 3b). The ages are all concordant.

Samples SH01, LD8, and LD9 had low zircon recovery, but the zircons are usually euhedral. Most of the zircons show clear oscillatory zoning without inherited cores, but inherited cores can be found in some zircons. For sample SH01, seven spot analyses of four individual zircon grains (combined rim and core analyses of some individual grains, same for below) provide a weighted mean age of 63.9 ± 0.7 Ma (2σ , MSWD = 1.0), with individual zircon dates ranging from 61.4 to 65.0 Ma (Figure 3c). The ages are all concordant. Moreover, three spot analyses of two zircon grains yield concordant Proterozoic ages, and one zircon yields a concordant Miocene age (Figure 3d; Table S3). For sample LD8, nine spot analyses of five individual zircon grains show a weighted mean age of 62.9 ± 1.5 Ma (2σ , MSWD = 0.7), with individual zircon ages between 60.2 and 65.9 Ma (Figure 3e). Three spot analyses of two zircon grains also yield concordant Proterozoic ages (Table S3). For sample LD9, however, five spot analyses of three individual zircon grains give a Miocene weighted mean age of 12.6 ± 0.8 Ma (2σ , MSWD = 0.2), with individual zircon ages ranging from 12.4 to 13.4 Ma (Figure 3f). Concordant old ages >400 Ma are also found (Table S3). These old ages (>400 Ma) probably represent the recycling of old continental crust during the formation of E_{1d} volcanic rocks. Both samples SH01 and LD9 were collected within the lower part of E_{1d} , and together with the presence of inherited cores, we believe that the young dates are meaningful and represent Miocene intrusions that cut the lower part of E_{1d} .

Comparison of the $^{40}\text{Ar}/^{39}\text{Ar}$ ages of samples GS1–4 and GS124 to the U-Pb zircon ages of the same samples shows that the $^{40}\text{Ar}/^{39}\text{Ar}$ ages and U-Pb zircon ages of these samples are consistent within error. By combining our results with other published radiometric ages from the Linzhou basin [*BGMXRAR*, 1993;

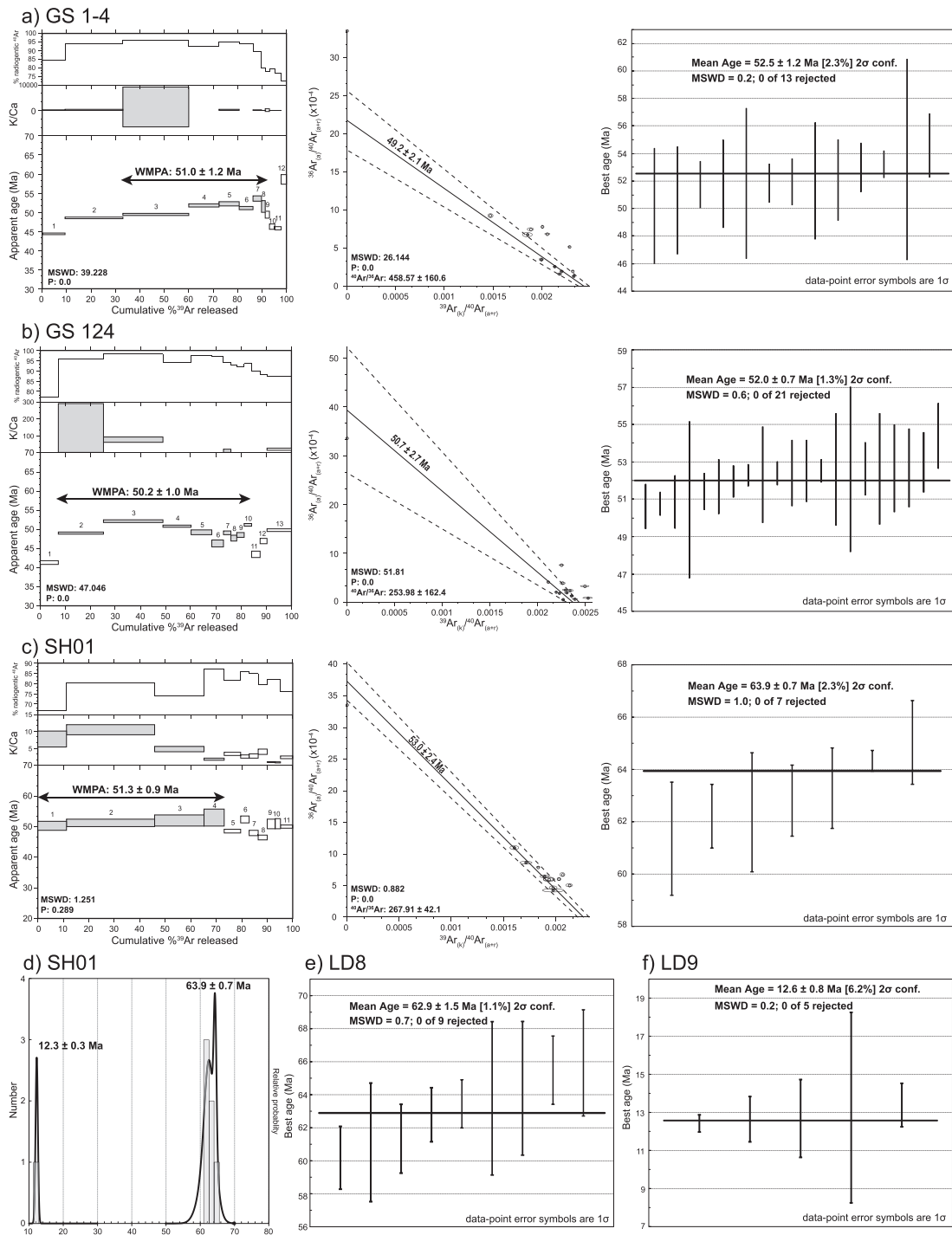


Figure 3. (a–c) $^{40}\text{Ar}/^{39}\text{Ar}$ and U–Pb zircon dating of the volcanic samples collected from both E_{2p} (GS1–4 and GS124) and E_{1d} (SH01) of the Linzong Group in the Linzhou basin. (d) Cumulative age probability plot of dating results of SH01; a single zircon crystal gives concordant Miocene age in addition to the results. (e) Individual zircon analyses of LD8 from top of the E_{1d} . (f) Individual zircon analyses of LD9 above the Cretaceous redbeds yield Miocene ages.

Zhou et al., 2004; He et al., 2007; Ding et al., 2014], we conclude that the E_{2p} volcanic rocks were emplaced between about 54 and 48 Ma. In contrast, the $^{40}\text{Ar}/^{39}\text{Ar}$ age of samples SH01 from E_{1d} is more than 10 Myr younger than the corresponding U–Pb zircon age; it is almost indistinguishable from the eruption ages of the overlying E_{2p} volcanic rocks. We therefore argue that the $^{40}\text{Ar}/^{39}\text{Ar}$ system of the E_{1d} volcanic rocks was

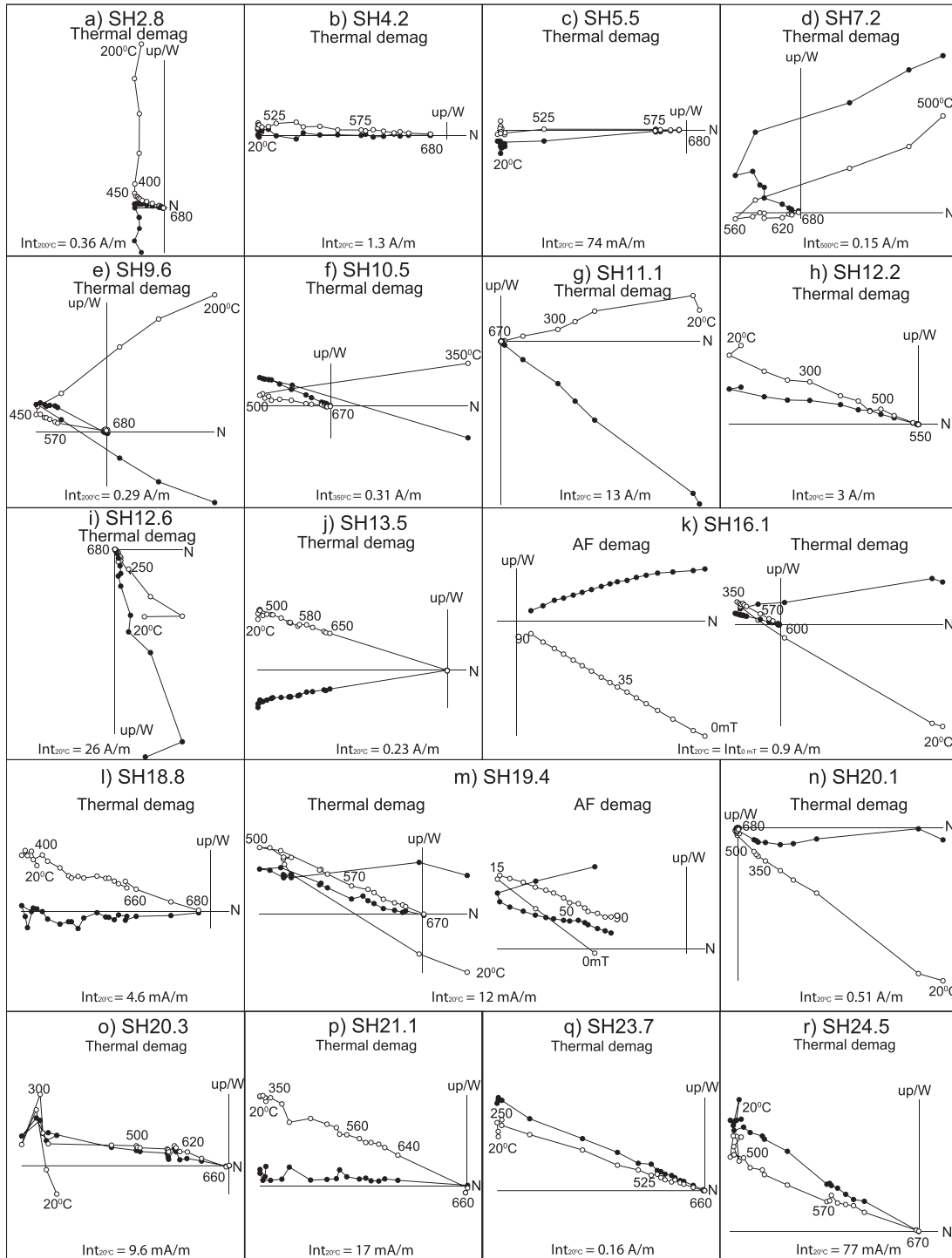


Figure 4. Demagnetization diagrams for samples representing the entire E_{1d} interval. All diagrams are displayed after bedding tilt correction. Closed (open) symbols represent the projection of vector end-points on the horizontal (vertical) plane; values represent alternating field and thermal demagnetization steps in milliTesla (mT) and °C, respectively. Most of the samples only yielded interpretable results when processed with thermal demagnetization (a–j and i–r); AF demagnetization can only remove part of the low-temperature component (e.g., SH16.1 in k). Few samples (SH19.4, m) yield comparable characteristic remanent magnetizations by AF and thermal treatments.

disturbed by post-emplacement thermal events. The U-Pb zircon ages in our study confirms that E_{1d} volcanic rocks erupted between ~68 and 62 Ma [Zhou *et al.*, 2004; He *et al.*, 2007; Lee *et al.*, 2007]. We also note the presence of Miocene intrusions (~13 Ma), which are widespread in the Lhasa terrane [e.g., Coulon *et al.*, 1986; Ding *et al.*, 2003] but which have never been reported in the Linzhou basin.

5. Paleomagnetism

5.1. Demagnetization

We isolated ChRM directions using both thermal and alternating field (AF) demagnetization techniques. Specimens were heated and cooled in a magnetically shielded ASC oven (Model TD48-SC) that has a residual field of <10 nT. The natural remanent magnetization (NRM) was measured on a horizontal 2G Enterprises DC SQUID magnetometer (noise level 3×10^{-12} Am²). Samples were progressively demagnetized by temperature steps at 100°C, 200°C, 250°C, 300°C, 350°C, 400°C, 450°C, 500°C, 525°C, 540°C, 550°C, 560°C, 570°C, 575°C, 580°C, 600°C, 620°C, 640°C, 650°C, 660°C, 670°C, and 680°C. AF demagnetizations were applied with an in-house-developed robotized sample handler [Mullender *et al.*, 2005] attached to a horizontal pass-through 2G Enterprises DC SQUID magnetometer (noise level 1×10^{-12} Am²) hosted in the magnetically shielded room (residual field <200 nT) at the Fort Hoofddijk Paleomagnetic Laboratory, Utrecht University (Netherlands). AF treatment consisted of successive steps of 5, 10, 15, 20, 25, 30, 35, 40, 45, 50, 55, 60, 65, 70, 80, and 90 mT.

For samples from E_{1d} , three NRM components were isolated by thermal demagnetization. The first component was commonly removed below 350°C (Figure 4). After removing this low-temperature component (LTC), an intermediate temperature component (ITC) was usually unblocked by 560°C–570°C, and a high-temperature component (HTC) was unblocked at 670°C–680°C (Figure 4). The ITCs and HTCs share a similar ChRM direction. We note that not every specimen recorded each of these three components. For some samples, only the first component was isolated; in some samples, the first and second were isolated; and in other samples, all the three components were isolated (Figure 4). For most samples, AF treatment was ineffective at isolating the ChRM. Only a few samples processed by AF treatment record a similar demagnetization trajectory as observed with thermal treatment, but this direction did not decay toward the origin of orthogonal vector plots (Figure 4m).

5.2. ChRM Directions

Principal component analysis [Kirschvink, 1980] on at least five successive steps resulted in precisely determined ChRM directions for most specimens (Table S4). All ChRM directions are calculated from the thermal demagnetization results because the AF treatment was ineffective at thoroughly demagnetizing the samples. Directions with mean angular deviations $>5^\circ$ were systematically rejected from further analysis (Table S4). Lava site-mean directions with $k < 50$ and $n < 5$ were systematically discarded following volcanic data selection criteria of Johnson *et al.* [2008] and Biggin *et al.* [2008]. These criteria are consistent with the selection criteria detailed in Lippert *et al.* [2014] (Table S5). Fisher [1953] statistics were used to evaluate the Virtual Geomagnetic Poles (VGPs) computed from the interpreted ChRM directions; site mean VGPs located more than 45° from the formation mean VGP were excluded from final direction calculations following the rationale of Johnson *et al.* [2008].

We isolated an LTC in 101 cores from all 24 sites, which together provided a mean direction of $D_g = 0.8^\circ$, $I_g = 41.1^\circ$ ($n = 81$, $k = 11.7$, $a_{95} = 4.8^\circ$) after applying 45° cut-off to these individual directions (Figure 5a). The ITC and HTC are often similar to each other. The overall mean ChRM direction of the 13 sites from E_{1d} that pass our data selection criteria is $D_g = 195.9^\circ$, $I_g = -25.4^\circ$ before tilt correction and $D_s = 193.5^\circ$, $I_s = -11.6^\circ$ ($k = 35$, $a_{95} = 7.1^\circ$, $\Delta D = 6.1^\circ$, $\Delta I = 11.8^\circ$) (Figures 5b and 5c; Table S5).

These ChRM directions are statistically indistinguishable from the 13 sites passing our selection criteria from E_{1d} that were reported by Chen *et al.* [2010] and Chen *et al.* [2014] (xl40–49, xl68–70, and xl145–156) (Figure 5c). This follows from a positive common true mean direction test (classification of "C") [McFadden and Lowes, 1981] between the 13 sites from this study and the 13 sites from Chen *et al.* [2010] and Chen *et al.* [2014]. We cannot evaluate whether the isolated ChRM directions from E_{1d} are primary or not with standard field tests because bedding attitude variations are minimal throughout the sampled succession; a fold test applied to the directions would have little, if any, geologic rigor. Moreover, each of the ChRM directions is of exclusively reversed polarity, which precludes a paleomagnetic reversal test.

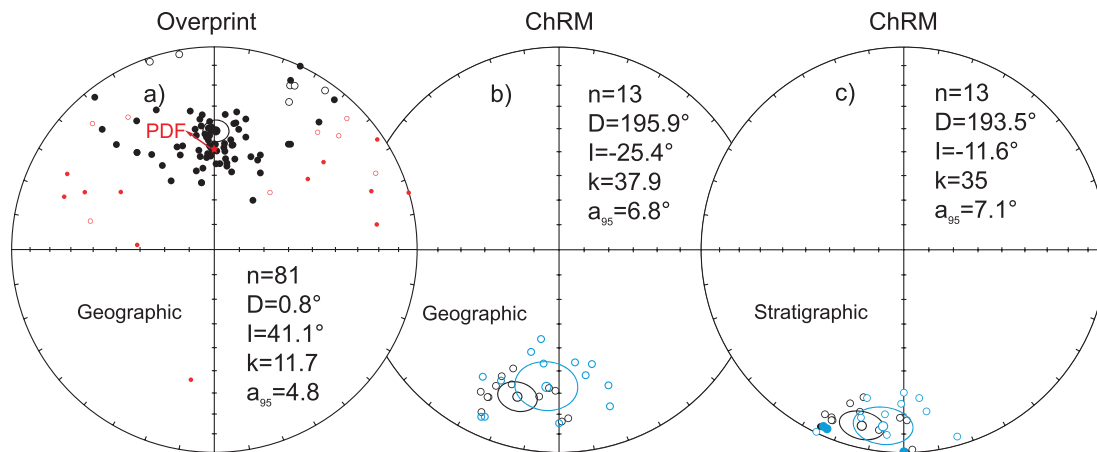


Figure 5. (a) Equal-area projections of the isolated low-temperature component in geographic coordinates. Red dots (circles) are rejected by the 45° cut-off criterion. (b and c) Equal-area projections of site-mean ChRM directions before [IS, b (“geographic” on the figure itself)] and after [TC, c (“stratigraphic” on the figure itself)] bedding tilt correction for volcanic sites from E_{1d}. Blue circles are the results from volcanic rocks from E_{1d} reported by *Chen et al.* [2010] and *Chen et al.* [2014]. The common true mean direction test of the mean directions from the two studies after tilt correction is positive with classification of “C” [McFadden and Lowes, 1981]. Star represents present day magnetic field (PDF) at the sample locality.

Results from the stratigraphically higher unit E_{2p} reported by *Dupont-Nivet et al.* [2010b] and *Huang et al.* [2013] also do not allow us to apply paleomagnetic field tests because of uniform bedding orientations and a limited number of sites with reversed polarity. However, a comparison of the ChRM directions from the E_{1d} volcanic rocks reported here with those reported from E_{2p} volcanic rocks and inclination shallowing-corrected sedimentary rocks yields a discrepancy of ~30° in inclination [Dupont-Nivet et al., 2010b; Huang et al., 2013]. Below, we explore possible causes for this large difference in inclination in rocks with ages within 10 Myr of each other. We measured the anisotropy of the magnetic susceptibility (AMS) of the sampled E_{1d} volcanic rocks to test whether inclination shallowing could be related to magnetic fabrics as it has been shown for some tuffs [Rochette et al., 1999; Callot et al., 2001; Callot and Geoffroy, 2004; Schöbel and de Wall, 2014]. Secondly, we provide a detailed rock magnetic analysis along with petrographic investigations of E_{1d} and E_{2p} samples to identify potential remagnetization processes as was revealed in other Linzizong volcanic successions in the Nanmulin basin [Huang et al., 2015b].

6. Rock Magnetism

We applied a bevy of rock magnetic analyses, including AMS, thermomagnetic experiments, hysteresis measurements, FORC diagrams, and component analysis of the IRM [Kruiver et al., 2001] to identify the magnetic fabric and the remanence carrier(s) of the E_{1d} volcanic rocks. Analytical methods can be found in supporting information.

6.1. Anisotropy of Magnetic Susceptibility

The AMS of 138 volcanic specimens from E_{1d} were measured. The susceptibility of the E_{1d} volcanic rocks varies considerably from 3.6×10^{-5} to 7.6×10^{-2} SI (Table S6). The degree of anisotropy (*P* value) is low, ranging from 1.002 to 1.048, with a mean of 1.017 (Table S6). The lavas do not exhibit uniformly oriented characteristic lineation (*L*) or foliation (*F*) (Figure 6a), and the magnetic fabric is neither dominantly oblate nor prolate (Figure 6b). The samples’ three principal ellipsoid axes (*K*_{max}, *K*_{int} and *K*_{min}) are distributed randomly in the stereoplots (Figures 6c and 6d), confirming that no discernible fabric can be identified at the site level. These characteristics are very similar to those from our AMS studies of E_{2p} volcanic rocks but are very different from those of E_{2p} sedimentary rocks [Huang et al., 2013], as well as some pristine igneous rocks (e.g., basalt) that record a magnetic fabric possibly induced by flow dynamics during the cooling of magma and secondary processes such as mineral growth during hydrothermal alteration and tectonic fracturing or deformation [MacDonadl and Palmer, 1990; Hargraves et al., 1991; Just et al., 2004; de Wall et al., 2010; Schöbel and de Wall, 2014]. We conclude that it is very unlikely that the paleomagnetic directions isolated from both E_{1d} and E_{2p} volcanic rocks are influenced by a preferred orientation of the magnetic minerals.

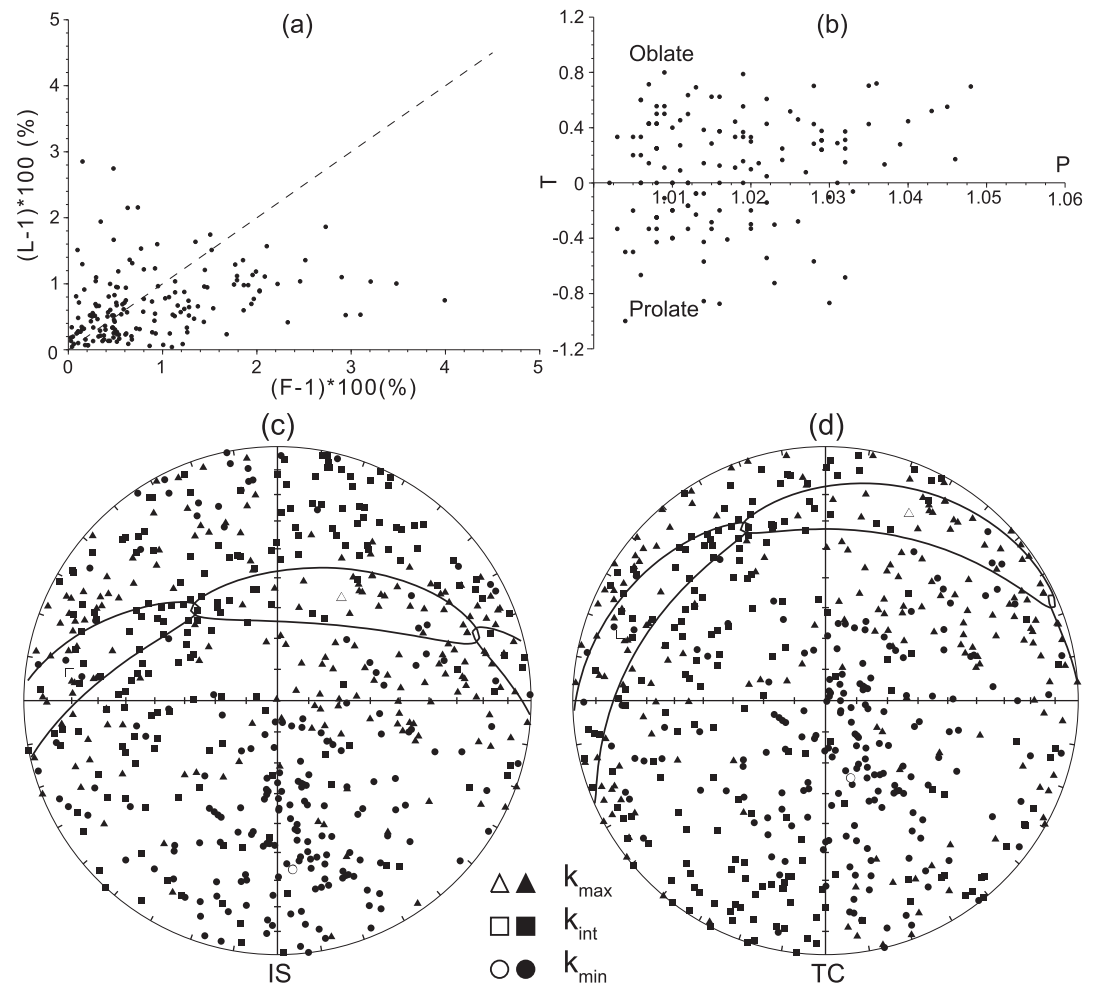


Figure 6. Magnetic anisotropy of E_{1d} volcanic rocks from AMS measurements. (a) Lineation (L) versus Foliation (F) diagram. (b) P versus T plot. $P = K_{max}/K_{min}$, $F = K_{int}/K_{min}$, $L = K_{max}/K_{int}$, $T = (\ln F - \ln L)/(\ln F + \ln L)$ [Jelinek, 1981]. (c and d) Stereoplots (equal-area, lower-hemisphere projection) showing AMS data of E_{1d} volcanic rocks. Maximum, intermediate, and minimum principal anisotropy axes are indicated, respectively, by triangles, squares, and circles. Open symbols are mean directions, with 95 percent confidence zones indicated. TC, tilt correction; IS, in situ (without tilt correction).

6.2. Thermomagnetic Runs

Twenty representative samples of different rock types representing the entire E_{1d} volcanic section were subjected to high-field thermomagnetic experiments. Typical results for volcanic samples from E_{1d} show a rapid decrease in saturation magnetization up to $\sim 350^\circ\text{C}$, $\sim 580^\circ\text{C}$, and/or $\sim 680^\circ\text{C}$ (Figures 7a–7c). In general, three magnetic mineral phases corresponding to the three NRM components isolated during thermal demagnetization can be distinguished by clearly steeper decreases in magnetization slope of the thermomagnetic runs: LTC ($\sim 250\text{--}350^\circ\text{C}$), ITC ($\sim 525\text{--}580^\circ\text{C}$), and HTC ($\sim 620\text{--}680^\circ\text{C}$) (Figures 7a–7c). The contribution of each component to the magnetization varies from sample to sample. The observed decreases around 350°C and around 580°C in magnetization for samples from the lower part of E_{1d} (SH9.7) define the LTC and ITC (Figure 7a). Samples from the upper part of E_{1d} (SH18.8 and SH24.7) are characterized by the appearance of the HTC in addition to the LTC and ITC (Figures 7b and 7c). We interpret the LTC to be associated with Ti-rich titanomagnetite and the ITC to be Ti-poor titanomagnetite, and the HTC is interpreted to be carried by hematite following Dunlop and Ödemir [1997].

6.3. Hysteresis Loops, IRM and Back-Field Curves, and FORC Diagrams

Hysteresis measurements were applied to 13 representative samples of different lithologies. We observed two distinctive types of hysteresis loops for samples from E_{1d} . Type 1 loops are narrow and are essentially saturated at

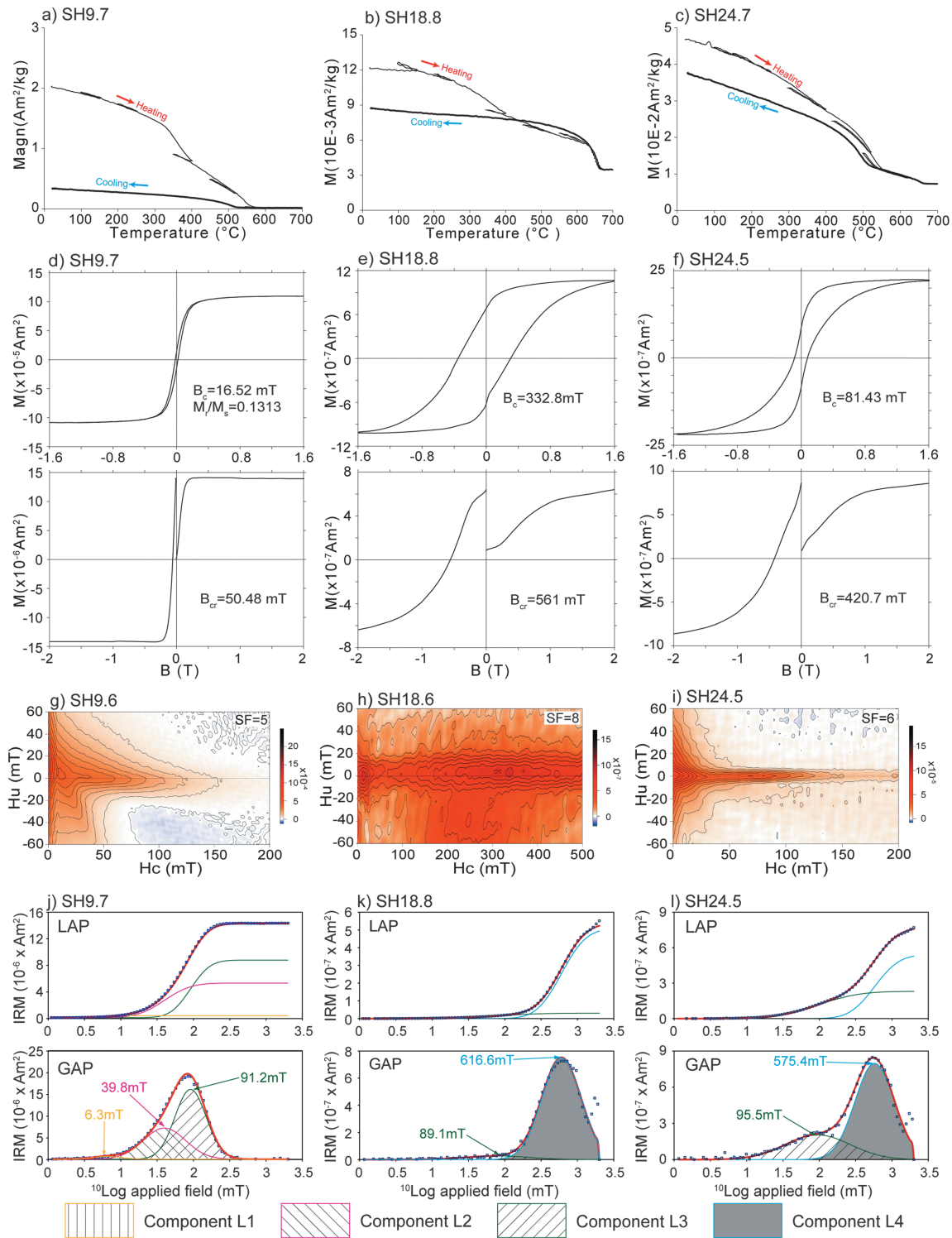


Figure 7. (a–c) High-field thermomagnetic runs on a modified horizontal translation Curie balance for typical samples from E_{1d} . Thin (thick) lines represent the heating (cooling) curves, which are also indicated by the arrows (heating: red, and cooling: blue). (d–f) Hysteresis loops, IRM, and back-field curves for characteristic samples from E_{1d} . Hysteresis loops are corrected for the paramagnetic contribution. The sample codes are indicated at the top of each diagram, and the hysteresis parameters are provided in the bottom-right part of the panels (M_s : saturation magnetization, M_r : remanent saturation magnetization, and B_c : coercive force). (g–i) First-order reversal curve (FORC) diagrams for typical samples processed with FORCinel 2.0 [Harrison and Feinberg, 2008]. The applied smoothing factor (SF) is marked in the top-right part of each diagram. (j–l) Representative examples of the IRM component analysis [Kruiver et al., 2001]. Four components (components L1–L4) are required to fit the IRM curves. Squares are measured data points. The components are marked with different lines: the linear acquisition plot (LAP) and the gradient acquisition plot (GAP) are shown in hatches.

600 mT (Figure 7d). The corresponding IRM curves are also completely saturated by 600 mT (Figure 7d). Bulk coercivity (B_c) values and remanent coercivity (B_{cr}) values of the samples are usually low (<60 mT) (Table S7). Type 2 loops are generally wasp waisted (Figures 7e and 7f), reflecting the presence of two or more magnetic components with strongly contrasting coercivities [Roberts *et al.*, 1995; Tauxe *et al.*, 1996]. IRM acquisition curves remain unsaturated up to 2 T, indicating the presence of high coercivity minerals (Figures 7e and 7f). Both B_c values and B_{cr} values are high, ranging from ~44 to 330 mT and from ~85 to 560 mT, respectively (Table S7).

Similar to our observations of the hysteresis loops, we distinguish two distinct groups of FORC diagrams. The FORC diagrams for samples with type 1 loops are characterized by contours that diverge away from the origin and are spread along the H_u axis (Figure 7g). This contour pattern is consistent with the typical behavior of interacting pseudo-single domain (PSD) to multiple domain (MD) magnetic particles [Pike *et al.*, 1999; Roberts *et al.*, 2000]. The FORC diagrams of samples with type 2 loops are characterized by the appearance of two contributions with different coercivities (Figures 7h and 7i). A dominant population of SD or PSD grains with very low coercivity is apparent along $H_u = 0$ mT is shown, but an additional contribution with distinctly higher coercivities and negligible magnetic interaction is also clearly displayed. We interpret the SD and PSD-MD magnetic particles with low to intermediate coercivities to be titanomagnetite, whereas magnetic particles with high coercivity are inferred to be hematite. These interpretations are consistent with the thermomagnetic data described in section 6.2.

6.4. IRM Component Analysis

In general, the IRM acquisition curves are preferably fit by four IRM components: component L1 with $B_{1/2}$ (the field at which half of saturation isothermal remanent magnetization (SIRM) is reached) of ~10 mT and dispersion parameter (DP) of ~0.35 (log units); a soft component L2 with $B_{1/2}$ ranging from 25 to 35 mT and DP varying from 0.22 to 0.35; a relatively hard component L3 with higher $B_{1/2}$ (50–150 mT) and notably variable DP (0.14–0.45); and a much harder component L4 with $B_{1/2}$ more than 400 mT and a DP of ~0.25 (Figures 7j–7l; Table S8). Component L1 with very low coercivity constitutes only a few percent of the SIRM; it is only required to fit the skewed-to-the-left distribution of component L2 and is not given physical meaning other than being the result of thermally activated component L2 particles [Egli, 2004; Heslop *et al.*, 2004]. We interpret component L2 and component L3 to represent Ti-poor titanomagnetite and Ti-rich titanomagnetite, respectively. These two components carry ~75%–100% of the SIRM for most samples in the lower part of E_{1d} (Table S8). The high dispersion parameter of these components suggests a broad magnetic grain-size distribution. We interpret component L4, with its very high coercivity, to be hematite. It contributes up to 96% of the SIRM for samples in the upper part of E_{1d} (Table S8).

These interpretations of the IRM component analysis are consistent with results from our other rock magnetic experiments. Ti-poor and Ti-rich titanomagnetite are the dominant magnetic carriers for samples from the lower part of E_{1d} . In contrast, samples from the upper part of E_{1d} are characterized by large amounts of hematite contributing to the SIRM.

7. End-Member Modeling of Magnetic Components

To illustrate the mechanism of remanence acquisition and to detect potential remagnetization of the Linzizong Group volcanic rocks from both E_{1d} and E_{2p} , we applied the method of end-member modeling of magnetic components as retrieved from IRM acquisition curves [Gong *et al.*, 2009b]. End-member modeling can be helpful for identifying remagnetized and non-remagnetized sedimentary rocks independent of paleomagnetic field tests [Gong *et al.*, 2009b; Van Hinsbergen *et al.*, 2010; Meijers *et al.*, 2011; Dekkers, 2012; Aben *et al.*, 2014; Huang *et al.*, 2015a, 2015c]. Our concomitant work on the Linzizong Group in the Nanmulin basin has shown that it is also a powerful tool for diagnosing remagnetization in volcanic rocks [Huang *et al.*, 2015b].

We measured IRM acquisition curves for 123 volcanic samples covering the entire sampled E_{1d} interval and 153 volcanic samples covering the entire E_{2p} interval. Procedures of the measurement and data analysis are the same as those described in Huang *et al.* [2015b].

7.1. Volcanic Rocks From E_{1d}

For samples from E_{1d} , the calculated two end-member model by the end-member solutions has a low r^2 value of 0.60219. The three end-member model has an r^2 value of 0.82727 and a convexity of -2.4634

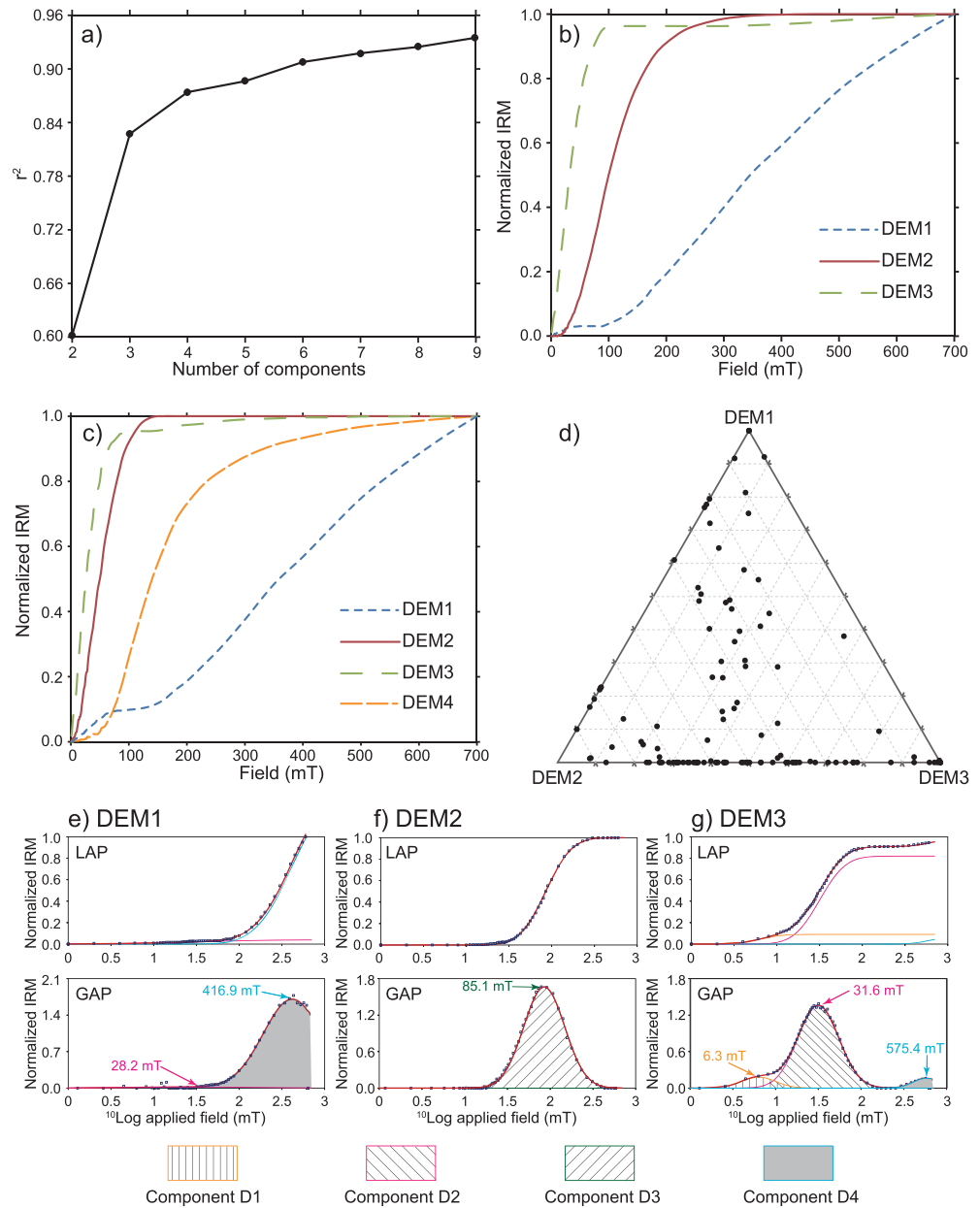


Figure 8. End-member modeling for volcanic rocks from E_{1d} . (a) Diagram showing the r^2 versus number of end members. (b and c) End members for the normalized IRM acquisition curves in the (b) three and (c) four end-member models. (d) Ternary plot of the three end-member model showing the end-member percentages for individual specimens. (e–g) IRM component analysis [Kruiver *et al.*, 2001] of the end members in the preferred three end-member model. Squares are the calculated data points from end-member modeling that are used to fit the IRM components. The components are marked with different lines: the linear acquisition plot (LAP) and the gradient acquisition plot (GAP) are shown. Component D1 has a very low coercivity and contribution; it is not assigned a physical meaning. Components D2 and D3 are harder; they represent Ti-poor and Ti-rich titanomagnetite, respectively. Component D4 has the highest coercivity and shows properties characteristic of hematite. IRM is normalized to the highest IRM value ($IRM/IRM_{700\text{ mT}}$); $\log_{10}(B_{1/2})$ and DP are in \log_{10} mT. Values of $B_{1/2}$ are displayed on each panel.

(Figure 8a). The four end-member model has an even higher r^2 of 0.87399 but a lower convexity of -2.0566 (Figure 8a). Models with five or more end-members are characterized by virtual duplication of end members, which indicates that the dataset is over-interpreted in these scenarios. Comparison of the models with three and four end members shows that the end members DEM1 (D stands for “Dianzhong Formation”) and

DEM3 are indistinguishable for both options, whereas DEM2 in the three end-member model is divided into DEM2 and DEM4 in the four end-member model (Figures 8b and 8c). This indicates that the four end-member model does not discriminate more distinctive and geologically interpretable end members than the three end-member model. Moreover, a break in slope is observed at three end members in the plot of r^2 versus the number of end members (Figure 8a). We therefore use the three end-member model to interpret our dataset from the E_{1d} volcanic rocks.

We applied IRM component analysis to these three end members [Kruiver *et al.*, 2001]. Four components (components D1 through D4, increasing from soft to hard magnetically) are required to fit the normalized IRM acquisition curves of the three end members. DEM1 can be fit with two components (component D2 and component D4; Figure 8e). Component D2 with $B_{1/2}$ of ~ 30 mT typically represents Ti-poor titanomagnetite [Day *et al.*, 1977; Lowrie, 1990]. The contribution of this component to SIRM is very low ($\sim 3\%$). Component D4 is probably hematite as indicated by the high $B_{1/2}$ of ~ 420 mT [Kruiver and Passier, 2001]. It contributes more than 95% to the SIRM (Table S8). The contribution of D2 to SIRM is very low ($\sim 3\%$). End-member DEM2 can be fit with component D3. We interpret it to be Ti-rich titanomagnetite, because of the fairly high $B_{1/2}$ of ~ 90 mT [Day *et al.*, 1977; Lowrie, 1990] (Figure 8f). The IRM acquisition curve for DEM3 requires three IRM components for a good fit: component D1, a very low coercivity component, constitutes $\sim 10\%$ of the SIRM; it is only required to fit the skewed-to-the-left distribution of component D2 and is not given physical meaning other than being the result of thermally activated component D2 particles [Egli, 2004; Heslop *et al.*, 2004]. Component D2 and component D4 typically represent Ti-poor titanomagnetite and hematite, respectively [Day *et al.*, 1977; Lowrie, 1990; Kruiver and Passier, 2001]. The contribution of component D2 to the SIRM is up to 85%, and component D4 has a limited contribution to the SIRM of $\sim 6\%$ (Figure 8g; Table S8). Inspection of the IRM component analysis of the end members shows that the four components required to fit them are indistinguishable from those components for the IRM acquisition curve fitting described in our rock magnetic studies above. This implies that the three end members are geologically meaningful [Weltje, 1997].

Most samples from E_{1d} are mixtures of the three end members in the ternary plot (Figure 8d). However, the contribution of DEM1 varies widely, and the contribution of DEM3 is usually limited (Figure 8d). There are also several samples that plot on the baseline between DEM2 and DEM3. Together with the above analysis for the mineralogic interpretation of the three end members, we conclude that magnetic carriers of the volcanic rocks from E_{1d} have variable contributions from hematite. Notably, the fraction of the remanence carried by hematite, as distinguished by end-member modeling, increases up-section toward the unconformity with E_{2n} .

7.2. Volcanic Rocks From E_{2p}

Similar to our observations from the volcanic rocks from E_{1d} , a three end-member model (PEM1 to PEM3, where P stands for "Pana Formation") is also preferred for the interpretation of the dataset from E_{2p} volcanic rocks (Figure 9); paleomagnetic results from which were previously reported by Dupont-Nivet *et al.* [2010b] and Tan *et al.* [2010]. The end members of these rocks also require four IRM components (components P1 through P4, increasing from magnetically soft to hard) for a good fit of the normalized IRM acquisition curves of the three end members. Components P1–P4 have the same physical meaning as components D1–D4 (Figures 9e–9g; Table S8). PEM1 represents a combination of hematite (contribution to SIRM up to $\sim 90\%$) and Ti-poor titanomagnetite (contribution to SIRM $\sim 10\%$, higher than that in DEM1) (Table S8). PEM2 is interpreted to be Ti-rich titanomagnetite. PEM3 is composed of Ti-poor titanomagnetite (contribution to SIRM approaching $\sim 90\%$) and minor contributions of hematite (contribution to SIRM around 5%).

In a ternary plot, most samples from E_{2p} are mixtures of PEM2 and PEM3 with minor contributions from PEM1 (Figure 9d). Moreover, careful inspection of the ternary plot reveals that more samples plot closer to PEM2 than PEM3, which indicates that the contribution of PEM2 is higher than that of PEM3 for most samples. Together with our above analysis that Ti-poor titanomagnetite also contributes $\sim 10\%$ to the SIRM in PEM1, we thus argue that titanomagnetite is the dominant magnetic carrier of the volcanic rocks from E_{2p} , whereas the contribution from hematite is minor. This conclusion is consistent with previously reported rock magnetic results from E_{2p} volcanic rocks [Dupont-Nivet *et al.*, 2010b; Huang *et al.*, 2013].

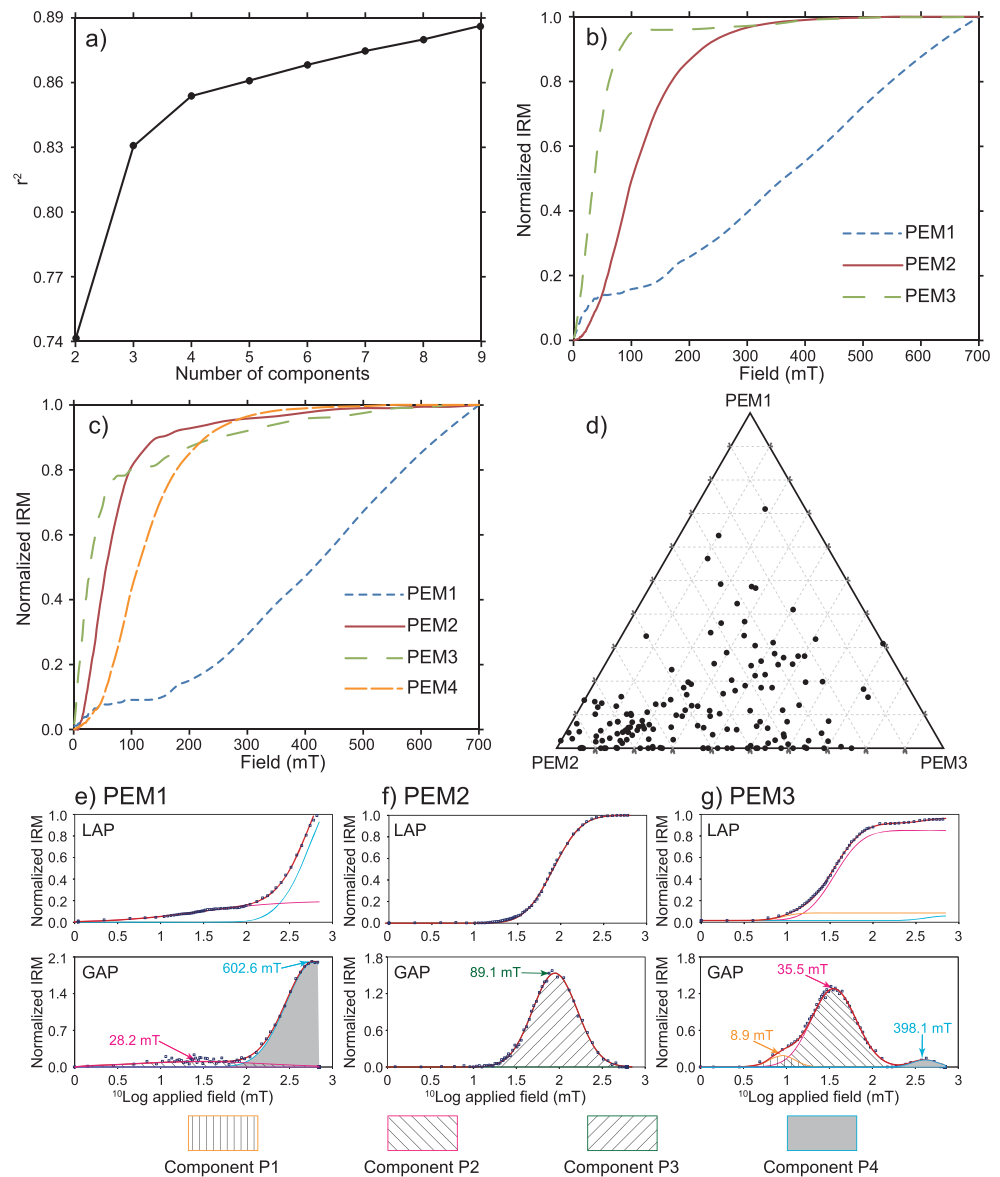


Figure 9. End-member modeling for volcanic rocks from E_{2p} . (a) Diagram showing the r^2 values versus the number of end members used to model the IRM. (b and c) End members for the normalized IRM acquisition curves in the three (b) and four (c) end-member models. (d) Ternary plot showing percentages of the three end members in the end members for each specimen. (e–g) IRM component analysis [Kruiver *et al.*, 2001] of the end members in the preferred three end-member model. Squares are the calculated data points from end-member modeling that are used to fit IRM components. The components are marked with different lines: the linear acquisition plot (LAP) and the gradient acquisition plot (GAP) are shown. Component P1 has a very low coercivity and contribution; it is not assigned a physical meaning. Components P2 and P3 are harder; they represent Ti-poor and Ti-rich titanomagnetite, respectively. Component P4 has the highest coercivity and shows properties characteristic of hematite. IRM is normalized to the highest IRM value ($IRM/IRM_{700\text{ mT}}$); $\log_{10}(B_{1/2})$ and DP are in \log_{10} mT. Values of $B_{1/2}$ are displayed on each panel.

8. Petrography

We analyzed thin sections of volcanic rocks from both E_{1d} and E_{2p} to identify textural relationships and diagenetic conditions of magnetic minerals with optical microscopy and SEM. Five representative samples from E_{1d} (SH2.8, SH5.5, SH18.4, SH18.6, and SH18.7) and four samples from E_{2p} (GL2.3, GL9.7, GL14.7, and GL29.4) were investigated by petrographic microscope. Five representative samples from E_{1d} (SH2.4, SH4.2, SH13.3, SH18.4, and SH24.8) and two samples from E_{2p} (GL8.5 and GL27.3) were also analyzed on a Hitachi

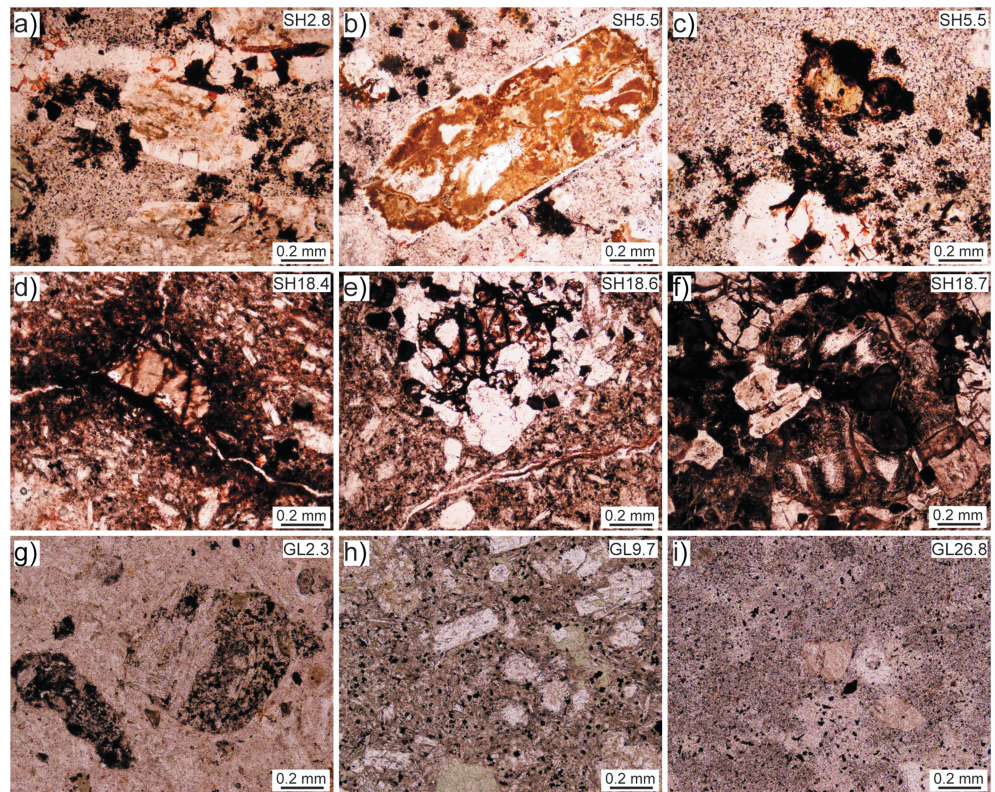


Figure 10. Thin section photographs of representative volcanic samples from both E_{1d} and E_{2p} under plane polarized light. (a–c) SH2.8 and SH5.5 from the lower part of E_{1d} , showing a porphyritic texture and alteration of feldspar lapillis and silicic matrix. (d) Precipitation of secondary hematite along a crack in the rock, with abundance decreasing inwardly in sample SH18.4 from the upper part of E_{1d} . (e and f) Secondary hematite is distributed along the cracks of the minerals in samples SH18.6 and SH18.7. (g) Ignimbrite sample GL2.3 from E_{2p} , showing a pyroclastic texture with scattered rock lapillis distributed in an ash matrix. (h and i) Ignimbrite samples GL9.7 (h) and GL26.8 (i) from E_{2p} with porphyritic texture show little sign of alteration.

S3400 SEM, operated at 20 keV and 40–60 nA at the Electron Microscope Unit at the University of Hong Kong (China).

8.1. Optical Petrography

Detailed petrographic observations of thin sections reveal that samples from E_{1d} are generally characterized by strong alteration, whereas the amount of alteration observed in samples from E_{2p} is low. Samples from E_{1d} are gray to reddish andesitic lavas. They have porphyritic texture with plagioclase/quartz phenocrysts distributed in a silicic matrix (Figures 10a–10f). Alteration of plagioclase to sericite is prevalent (Figures 10a–10f). Accessory minerals include biotite, epidote, rutile, and iron oxides. Opaque minerals (mostly hematite) are very common as accessory phases in all samples. Three distinct populations can be recognized. The first population consists of independent crystals distributed randomly within the matrix (Figures 10a–10c). A second population clusters at margins of preexisting minerals and appears to be an alteration product of biotite and feldspar (Figures 10a–10c and 10f). A third population consists of small grains distributed at margins of the silicate minerals or along the cracks (Figures 10d and 10e). The first and the second populations are very common in samples SH2.8 and SH5.5 (i.e., lower in the section), whereas the third population is dominant in samples SH18.4, SH18.6, and SH18.7 (i.e., higher in the section).

Samples from E_{2p} are tuff with a pyroclastic texture characterized by scattered lapilli distributed in an ash matrix, as described in detail by Huang *et al.* [2013] (Figures 10g–10i). Plagioclase is slightly altered to clay minerals, calcite, and chlorite. The opaque minerals [mostly (titano)magnetite] are common as an accessory phase in all the samples. They often occur as large isolated crystals distributed randomly within the ash matrix or clusters in the volcanic fragments.

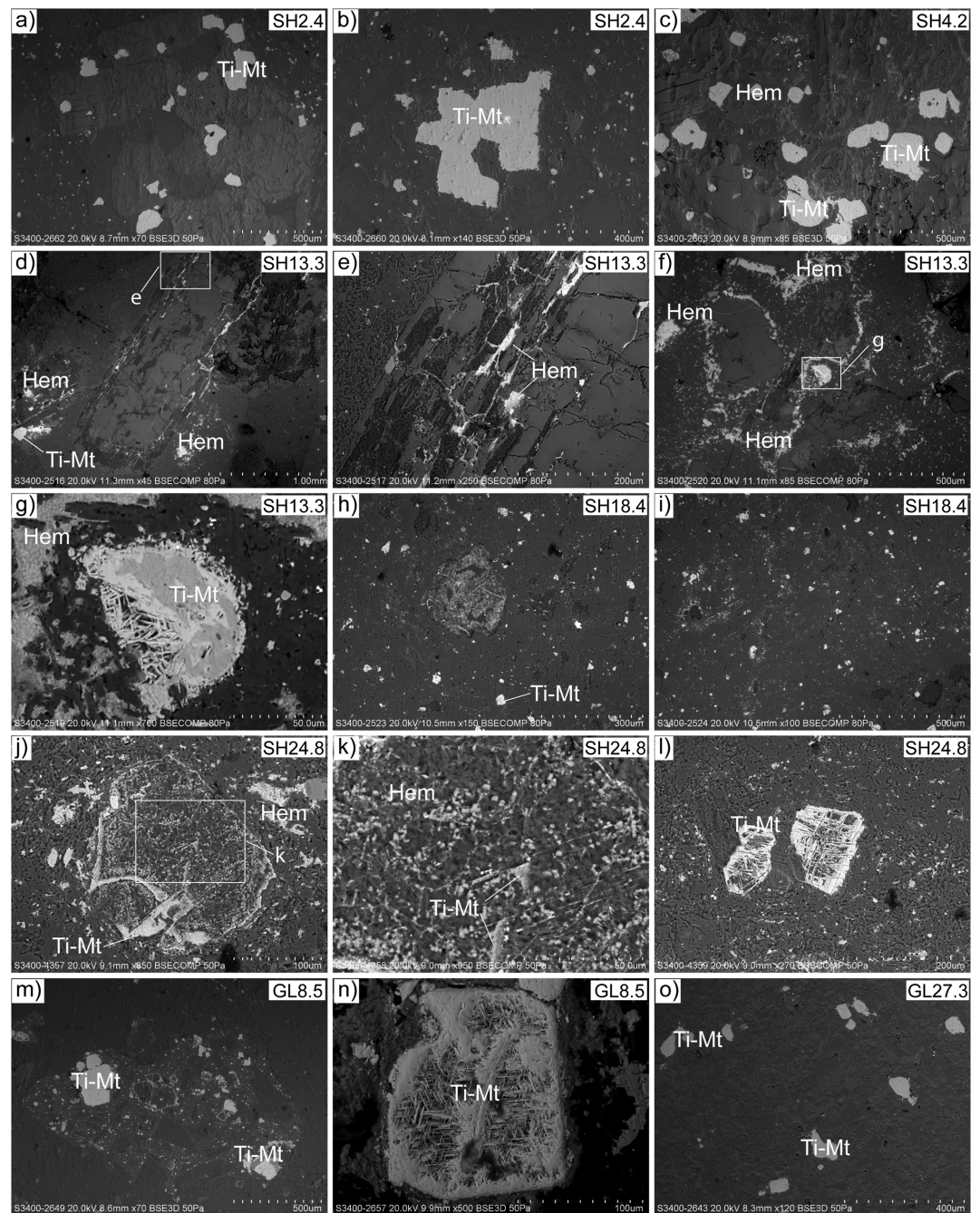


Figure 11. SEM back-scattered electron images for selected samples from both E_{1d} and E_{2p} . Hem: hematite, Ti-Mt: titanomagnetite. (a–c) Samples SH2.4 and SH4.2 from the bottom of E_{1d} , with abundant titanomagnetite particles showing solid-state exsolution features. (d–f) Hematite growing around or within the silicate minerals in sample SH13.3 from the middle part of E_{1d} . (g) High-magnification view of sample SH13.3 showing secondary hematite growth around a large titanomagnetite grain. (h and i) Small titanomagnetite particles with low abundance disperse in sample SH18.4, whereas fine hematite particles are everywhere. Also observed is hematite replacing a titanomagnetite grain with the original crystal habit of titanomagnetite retained in (h). (j and k) Alteration of titanomagnetite to fine-grained hematite in samples SH24.8 from the top of E_{1d} . (l) Euhedral titanomagnetite grains with typical solid-state exsolution features in sample SH24.8. (m) Titanomagnetite with variable grain sizes in the rock lapillis from ignimbrite sample GL8.5 from E_{2p} . (n) Large titanomagnetite grain with solid-state exsolution features in sample GL8.5. (o) Euhedral titanomagnetite grains in sample GL27.3 from E_{2p} .

8.2. SEM Observations

Additional textural information about the iron oxides is provided by SEM observations. Two types of iron oxides, titanomagnetite and hematite with contrasting petrographic features, are generally present in samples from E_{1d} . However, the abundances of titanomagnetite and hematite change from sample to sample. In samples SH2.4 and SH4.2 from lower in the section, titanomagnetite grains are abundant, whereas hematite is rarely observed. Titanomagnetite grains usually occur as euhedral to subhedral grains ranging in size from a few micrometers up to 500 μm (Figures 11a–11c). Most of the titanomagnetite grains show solid-state oxidation-exsolution features with a lamellae of ilmenite distributed in the Ti-poor magnetite. These textures indicate a magmatic origin [Craig, 2001; Turner *et al.*, 2008] (Figures 11a–11c). We also observe titanomagnetite with oxidation-exsolution features in samples SH13.3, SH18.4, and SH24.8, but note that the abundance is remarkably low (Figures 11d–11l). Hematite in our samples differs substantially from titanomagnetite: it has a different crystal habit and its distribution is also different. It is usually fine grained and occurs either intergrown within titanomagnetite grains (Figures 11f, 11g, 11j, and 11k), around the silicate minerals (Figures 11f), or along folia within the matrix and larger crystals (Figures 11d and 11e).

Titanomagnetite is abundant in samples from E_{2p} (Figures 11m–11o), compared to samples from the upper intervals of E_{1d} . Titanomagnetite grains occur in a range of sizes, from less than 10 μm to over 400 μm (Figures 11m–11o). They are concentrated in the lapilli (Figure 11m). The titanomagnetite grains are usually euhedral and exhibit oxidation-exsolution features. These observations suggest that the host tuff was formed during a slow-ascending eruption [Turner *et al.*, 2008] and that the titanomagnetite is primary.

These textural observations suggest that titanomagnetite has a magmatic origin, whereas hematite is secondary and formed authigenically after volcanism. Given that SEM observations indicate that titanomagnetite is the predominant iron oxide and end-member modeling of the magnetic components indicates that this titanomagnetite carries the bulk of the magnetic remanence in samples from E_{2p} volcanic rocks in the Linzhou basin, we conclude that, mineralogically, samples from E_{2p} volcanic rocks show minor to no signs of chemical alteration and thus remagnetization. In contrast, petrographic observations clearly indicate that hematite is of secondary origin, and we suspect that samples from E_{1d} with hematite as a significant remanence carrier likely records a secondary magnetization. That is, at least some, if not most, samples from E_{1d} in the Linzhou basin might be partially remagnetized, similar to what we found in the Nanmulin basin [Huang *et al.*, 2015b].

9. Discussion

9.1. The Case for Remagnetization

Inclination shallowing caused by sedimentary processes has been advocated to explain the shallow bias in paleomagnetic inclinations recorded by detrital sedimentary rocks [King, 1955; Løvlie and Torsvik, 1984; Anson and Kodama, 1987; Deamer and Kodama, 1990; Jackson *et al.*, 1991; Tauxe and Kent, 2004; Dupont-Nivet *et al.*, 2010a; Kodama, 2012]. However, volcanic rocks are, in principle, immune to inclination shallowing biases. Unlike the strongly shallowed inclinations in the sedimentary cover of the Low Cretaceous Xigaze ophiolites [Huang *et al.*, 2015a], the redbeds from the Upper Cretaceous Takena Formation [Tan *et al.*, 2010], and the sedimentary rocks from E_{2p} in the Linzhou basin [Huang *et al.*, 2013], the lavas of E_{1d} and E_{2p} do not have a characteristic magnetic anisotropy fabric that is consistent with flattening or an otherwise strong igneous fabric (Figure 6) [see also Huang *et al.*, 2013; Chen *et al.*, 2014].

Paleosecular variation (PSV) of the Earth's magnetic field can lead to an intrinsic variation of $>30^\circ$ in inclination in spot readings of the geomagnetic field [Johnson *et al.*, 2008; Tauxe *et al.*, 2008; Deenen *et al.*, 2011]. Large datasets from volcanic rocks in E_{2p} with a sufficiently long range of emplacement ages display directional distributions that suggest PSV is fully characterized [Dupont-Nivet *et al.*, 2010b; Lippert *et al.*, 2014]. These conclusions are further supported by the similarity between ChRM directions of the lavas from E_{2p} and the inclination shallowing-corrected sedimentary rocks from E_{2p} [Huang *et al.*, 2013].

The E_{2p} and E_{1d} volcanic deposits described here were dated using whole rock $^{40}\text{Ar}/^{39}\text{Ar}$ and zircon U-Pb geochronology from the same volcanic samples. For volcanic rocks from E_{2p} , the similarity between whole rock $^{40}\text{Ar}/^{39}\text{Ar}$ and zircon U-Pb ages suggests that thermal or chemical resetting is inconsequential. Our analyses based on rock magnetic investigations and petrographic observations also provide no evidence for substantial alteration and secondary magnetic mineral growth. Thus, there is no rock magnetic, mineralogic,

or geochronologic reason to doubt a primary origin of the NRM isolated from the E_{2p} volcanic rocks. In contrast, volcanic rocks from E_{1d} have whole rock $^{40}\text{Ar}/^{39}\text{Ar}$ ages that are statistically younger than the zircon U-Pb ages and that are of similar or even younger ages than ages of the overlying E_{2p} volcanic rocks. These observations indicate thermal and/or chemical resetting of the E_{1d} volcanic rocks. Together with the widespread secondary hematite growth revealed by our rock magnetic and petrographic investigations, we conclude that the NRM isolated from the E_{1d} volcanic rocks was acquired in part during post-depositional alteration. To summarize, the E_{1d} sequence has been remagnetized.

9.2. Potential Remagnetization Mechanisms

Acquisition of magnetization after the formation of a rock, termed remagnetization, can obscure or remove the primary magnetizations and thus limit the utility of paleomagnetism in global (plate) tectonic reconstructions [Elmore *et al.*, 2012; Font *et al.*, 2012]. Widespread remagnetization events are usually linked to large-scale tectonic processes [McCabe *et al.*, 1983; Miller and Kent, 1988; Chen and Courtillot, 1989; Appel *et al.*, 1995; Molina Garza and Zijdeveld, 1996; Weil and Van der Voo, 2002; Font *et al.*, 2006; Rapalini and Bettucci, 2008; Font *et al.*, 2012] and can affect both sedimentary rocks [Appel *et al.*, 1991; Gong *et al.*, 2009a; Roberts *et al.*, 2010; Liu *et al.*, 2011; van der Voo and Torsvik, 2012] and igneous rocks [Harlan *et al.*, 1996; Edel and Aifa, 2001; Geissman and Harlan, 2002; Otofujii *et al.*, 2003; Borradaile *et al.*, 2008; Preeden *et al.*, 2009]. Suspected mechanisms for remagnetization include elevated temperature, chemical alteration, and secondary mineral growth. These processes can act alone or in concert, and they frequently induce changes to the NRM, to the magnetic mineralogy, or both [Jackson and Swanson-Hysell, 2012].

9.2.1. Acquisition of Thermoviscous Remanent Magnetization

The volcanic record of the southern Lhasa terrane indicates a magmatic “flare-up” at ~ 51 Ma [Kapp *et al.*, 2007b; Lee *et al.*, 2009; Jiang *et al.*, 2014]. In the Linzhou basin, this flare-up is characterized by the eruption of large volumes of E_{2p} volcanic rocks, intrusion of dykes into E_{2nr} , E_{1d} , and the Cretaceous Takena Formation, and emplacement of granitic plutons into Triassic strata [Yue and Ding, 2006; He *et al.*, 2007]. Therefore, we must consider the regional thermal disturbance this volcanism and magmatism must have provided. This thermal disturbance could have had a strong effect on volcanic rocks from E_{1d} , given that the volcanic interval from E_{2p} (~ 1900 m) is much thicker than E_{1d} (~ 270 m) [He *et al.*, 2007] and that early Eocene dykes are widespread within E_{1d} (Figures 2h, 2j, and 2k). Our geochronologic studies of the E_{1d} lavas show a discrepancy of ~ 10 Myr between the U-Pb dates and $^{40}\text{Ar}/^{39}\text{Ar}$ dates (Figure 3c). Moreover, the $^{40}\text{Ar}/^{39}\text{Ar}$ ages of the E_{1d} lavas are similar to the ages of the dykes and E_{2p} tuffs, indicating that thermal disturbance of $^{40}\text{Ar}/^{39}\text{Ar}$ system of the E_{1d} volcanic rocks is probably induced by intrusion of the dykes and eruption of the overlying E_{2p} volcanic rocks. Therefore, we conclude that it is very likely that the conductive cooling of dykes and thick tuffs at ~ 52 Ma thermally activated the titanomagnetite grains to produce a thermoviscous remanent magnetization (TVRM) in the E_{1d} volcanic rocks.

Several studies have shown how remagnetization by TVRM has been acquired in rocks subjected to post-depositional thermal events [Kent, 1985; Kent and Miller, 1987; Smith and Verosub, 1994; Harlan *et al.*, 1996; Dunlop *et al.*, 1997; Valet *et al.*, 1998; Enkin *et al.*, 2000]. Acquisition of TVRM is based on the relationships between relaxation time and blocking temperatures [Néel, 1949; Pullaiah *et al.*, 1975; Middleton and Schmidt, 1982; Dunlop *et al.*, 2000], which implies that the primary NRM can be partially reset below the Curie temperature when the temperature is elevated for a sufficiently long duration. A secondary NRM can be acquired during subsequent (very slow) cooling from these elevated temperatures.

Given closure temperatures of the K-Ar system of ~ 300 – 350°C for biotite and of ~ 150 – 300°C for potassium feldspar [McDougall and Harrison, 1999], the disturbance observed in the whole rock $^{40}\text{Ar}/^{39}\text{Ar}$ system of the lava flows from E_{1d} suggests that these rocks probably have been heated up to $\sim 300^\circ\text{C}$. Assuming a minimum of 20 kyr duration for remagnetization (based on the assumption that secular variation has been adequately averaged), SD magnetite with maximum unblocking temperatures of 560 – 570°C (at laboratory heating time of 45 min, same for the following calculations) require temperatures $\geq 550^\circ\text{C}$ to completely reset the primary NRM [Pullaiah *et al.*, 1975]. However, the required temperatures could be $\sim 490^\circ\text{C}$ if the magnetite is of PSD size [Middleton and Schmidt, 1982]. The required temperature will be (much) lower if the maximum unblocking temperatures of (titano)magnetite decrease as a function of grain size or primary composition [Pullaiah *et al.*, 1975; Middleton and Schmidt, 1982]. For example, SD titanomagnetite and PSD titanomagnetite with maximum unblocking temperatures both of 500°C can be completely reset at $\sim 450^\circ\text{C}$ and $\sim 380^\circ\text{C}$, respectively, if the heating persists for 20 kyr. With an unblocking temperature

of $\sim 350^{\circ}\text{C}$, however, SD and PSD titanomagnetite can be completely reset at $\sim 260^{\circ}\text{C}$ and $\sim 180^{\circ}\text{C}$, respectively, if the higher temperature would have prevailed for as few as 100 years. We have detected both Ti-rich titanomagnetite (unblocked at 300°C – 350°C) and Ti-poor titanomagnetite (unblocked at 550°C – 570°C) with domain states of PSD-MD in our rock magnetic investigations (Figure 7). Therefore, we conclude that the primary NRM carried by Ti-rich titanomagnetite easily could have been overprinted by a secondary TVRM similar to the NRM recorded by E_{2p} volcanic rocks during the thermal disturbance. In contrast, only part of the primary NRM residing in Ti-poor titanomagnetite would have been overprinted by a similar TVRM. Thus, the isolated ITC carried by Ti-poor titanomagnetite is a combination of a predominantly primary NRM with reversed polarity and a minor TVRM with normal polarity, resulting in a composite direction that has a reversed polarity but a shallower inclination than the primary NRM.

Careful inspection of the isolated LTC, however, shows that its mean direction is shallower than both the NRM recorded by volcanic rocks from E_{2p} and the viscous overprint induced by the present day magnetic field (Figure 5a). It is actually very close to the NRM recorded by volcanic rocks from E_{2p} after tilt correction [Dupont-Nivet *et al.*, 2010b]. Given that PSD titanomagnetite with maximum unblocking temperatures of 350°C can be completely reset at $\sim 120^{\circ}\text{C}$ if heating persists for 100 kyr [Middleton and Schmidt, 1982], we suggest that it is likely that the TVRM recorded by Ti-rich titanomagnetite in E_{1d} at ~ 52 Ma could have been reset again whereas the NRM of the Ti-poor titanomagnetite was not significantly affected. This thermal event might be caused by Miocene intrusions in the lower part of E_{1d} (dated at ~ 13 Ma; Figures 3d and 3f). The acquisition of the new TVRM likely occurred after E_{2p} had been tilted $\sim 30^{\circ}$ toward the north. This new TVRM might also be carried by the dykes intruded in E_{1d} , because the in situ magnetization directions of the dykes are similar to that of the in situ LTC of the E_{1d} lavas; the magnetic carrier is Ti-rich titanomagnetite in both units [Liebke *et al.*, 2010; Liebke *et al.*, 2012].

9.2.2. Acquisition of Chemical Remanent Magnetization

We used the rock magnetic and petrographic studies described above to characterize the variable abundance of secondary hematite in some of the lavas from E_{1d} . These observations are similar to those of the partially remagnetized volcanic rocks of the Linzizong Group in the Nanmulin basin [Huang *et al.*, 2015b]. These similarities suggest that a chemical remanent magnetization (CRM) carried by the secondary hematite is responsible for at least some of the remagnetization. Post-eruptive precipitation and growth of hematite to produce CRMs during low-temperature hydrothermal alteration of igneous rocks has been described in several settings [Edel and Schneider, 1995; Edel and Aifa, 2001; Geissman and Harlan, 2002; Ricordel *et al.*, 2007; Preeden *et al.*, 2009; Parcerisa *et al.*, 2013]. For example, oxidizing hydrothermal fluids migrating along a structural or stratigraphic plane (e.g., unconformity, fault, fracture, and/or joint) can leach iron from magmatic (titano) magnetite and Fe-rich silicates in the igneous body; this iron can then precipitate as hematite at temperatures well below the Curie temperature [Elmore *et al.*, 1993; Dekkers, 2012; Elmore *et al.*, 2012]. The direction of the NRM carried by this secondary hematite can be very different from that of the primary remanent magnetization if this process happens after the tilting or large-scale tectonic motion of the terrane. Importantly, it does not matter whether the igneous rocks are completely or only partially remagnetized, the isolated ChRM cannot be used in a meaningful way for paleogeographic reconstructions.

Our rock magnetic studies suggest that the amount of secondary hematite decreases downward from the unconformity between E_{1d} and E_{2n} . This trend is consistent with remagnetization caused by paleoweathering and laterization of the lavas of E_{1d} due to percolation of meteoric water prior to deposition of E_{2n} [Schmidt *et al.*, 1976; Kumar and Bhalla, 1984; Kumar, 1986; Evans *et al.*, 2002; Théveniaut and Freyssinet, 2002]. This scenario is further supported by field observations that the lavas of E_{1d} are unconformably overlain by redbeds at the base of E_{2n} (Figures 2j–2l).

Alternatively, the remagnetization of E_{1d} could have been caused by migration of a high-temperature magmatic hydrothermal fluid along the base of the sedimentary strata from the lowermost E_{2n} and the unconformity between E_{1d} and E_{2n} during the eruption of the thick tuffs from E_{2p} at ~ 52 Ma. This event was accompanied by the intrusion of some of the dykes in E_{1d} and E_{2n} . Strong hydrothermal alteration of E_{1d} lavas is observed not only near the unconformity but also close to the dykes (Figure 2g).

We cannot rule out either of the two processes described above; in fact, we suspect that they worked in concert for the acquisition of CRMs for the reasons described next. During the demagnetization of the E_{1d}

volcanic rocks, the HTC carried by hematite is of reversed polarity with a low inclination. If the hematite formed during the paleoweathering and laterization between ~62 and ~54 Ma when E_{1d} was slightly tilted to the south by about 5° (the dip of the redbeds at the lowermost of E_{2n} strata is $\sim 5^\circ$ steeper than that of E_{1d}), then this hematite probably would have acquired a CRM similar to the primary magnetization with reversed polarity (i.e., Chrons C27r, C26r, C25r, or C24r; n.b.: intervals between ~62 and 54 Ma with normal magnetic polarity are very short) [Gradstein *et al.*, 2012]. This CRM should have recorded a steeper inclination than what we observe. However, if the hematite crystallized during the migration of magmatic hydrothermal fluid at ~52 Ma when E_{1d} was tilted $\sim 15^\circ$ toward the south (dip of E_{2p} rocks is $\sim 15^\circ$ steeper than that of E_{1d} ; Figure 1b), then we expect it to acquire a CRM similar to the TRM of E_{2p} . This CRM would have normal polarity and a very high inclination before tilt correction. We observe neither of these predictions. However, if both of the suggested processes are responsible for the CRM of E_{1d} , then we expect ChRM directions carried by secondary hematite to be similar to the directions we observe. Therefore, we favor a scenario in which the CRMs carried by the secondary hematite were acquired during two distinct events.

In summary, we suggest that the remagnetization of lavas from E_{1d} is a combination of TVRM and CRM acquisitions (Figure 12). We suggest that there were two episodes for the acquisition of TVRM (TVRM₁ and TVRM₂). In our scenario, TVRM₁ is carried by Ti-poor titanomagnetite and was induced by the thermal disturbance associated with the eruption of E_{2p} volcanic rocks and intrusion of dykes into E_{1d} (Figure 12c). TVRM₂ is carried by Ti-rich titanomagnetite and was acquired after E_{2p} had been tilted $\sim 30^\circ$ toward the north at ~13 Ma (Figure 12e). The CRM is carried by secondary hematite, which also may have been formed during two stages. The first stage for the acquisition of CRM (CRM₁) occurred sometime between ~62 and 54 Ma when E_{1d} was tilted $\sim 5^\circ$ toward the south and E_{2n} was deposited (Figure 12b). The second stage for the acquisition of CRM (CRM₂) probably occurred at the same time as TVRM₁ at ~52 Ma, during the eruption of E_{2p} and intrusion of dykes throughout E_{1d} . The E_{1d} sequence was tilted $\sim 15^\circ$ toward the south at this time (Figure 12c). We acknowledge that this sequence of events is non-unique and other remagnetization scenarios may explain the observed paleomagnetic data. Our intent is not to fully explain the events responsible for the remagnetization but to emphasize that the preponderance of field and laboratory observations indicates that the ChRM directions recorded in E_{1d} lavas are not primary. We have illustrated one plausible sequence of events that (1) can explain the observed directions, (2) is consistent with field observations and regional geochronology, and (3) can be tested with additional geochronology, thermochronology, and structural analysis.

9.3. Paleogene Latitude of the Lhasa Terrane and Implications for Constraining the Age of the India-Asia Collision

We have reassessed the paleomagnetic results of the Linzizong volcanic rocks in the Linzhou basin using detailed rock magnetic investigations, petrographic observations, and geochronologic data. Our analyses show that the discrepancy of $\sim 30^\circ$ in tilt-corrected inclinations between volcanic rocks from E_{1d} and E_{2p} is an artifact of an inappropriate tilt-correction applied to a secondary remanence in remagnetized rocks. Lavas from E_{1d} have been remagnetized by secondary CRMs and TVRMs, whereas volcanic rocks from E_{2p} do not show any evidence of secondary magnetic mineral growth or thermal resetting. Therefore, we conclude that ChRM directions from E_{1d} volcanic rocks in the Linzhou basin cannot be used to calculate the Paleogene latitude of the Lhasa terrane. Volcanic rocks from E_{2p} that do record a primary NRM and have a directional distribution that can be explained by paleosecular variation are interpreted to accurately record the Paleogene latitude of the Lhasa terrane. We assert that the mean inclination of $40.3 \pm 4.5^\circ$ (95% confidence limit) measured in the volcanic rocks of the E_{2p} unit is reliable for tectonic reconstructions [Dupont-Nivet *et al.*, 2010b]. Inclinations obtained from sedimentary rocks of the upper E_{2p} unit in the Linzhou basin that have been corrected for inclination shallowing using two independent correction methods $\{40.0^\circ$ [(33.1°, 49.5°), 95% confidence limit] and $41.3 \pm 3.3^\circ$ (95% confidence limit)} are indistinguishable from the primary E_{2p} volcanic rocks directions [Huang *et al.*, 2013]. We also note that our recent results from ~52 Ma volcanic rocks in the Nanmulin basin ~200 km to the west of the Linzhou basin suggest a primary inclination of 38.1° [(35.7°, 40.5°), 95% confidence limit] [Huang *et al.*, 2015b]. Collectively, these paleomagnetic results from the Linzizong Group indicate that the southern Lhasa terrane was located at $\sim 20 \pm 4^\circ\text{N}$ (assuming a 100% geocentric axial dipole field) during early Eocene time [BGMRXAR, 1993; Mo *et al.*, 2003; Zhou *et al.*, 2004; He *et al.*, 2007; Huang *et al.*, 2015b].

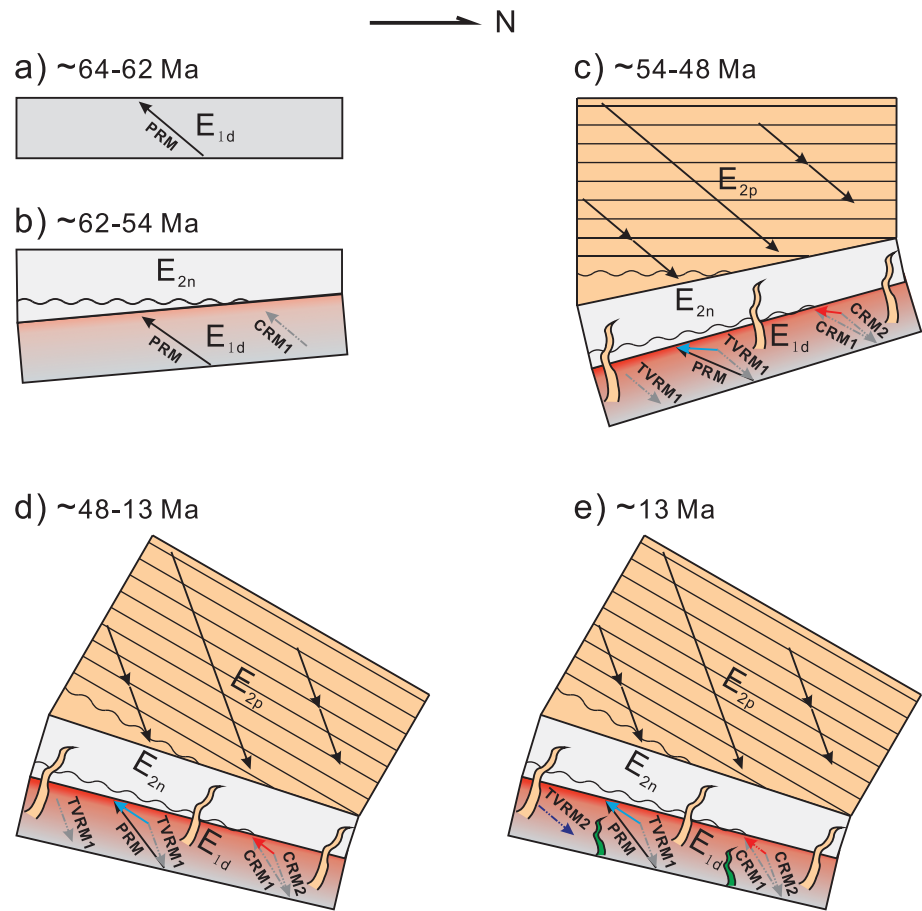


Figure 12. Possible sequence of events for the remagnetization of E_{1d} in the Linzhou basin in cross-section view. (a) Eruption of E_{1d} at ~64–62 Ma (Chron C26r or C27r) at ~20°N latitude; a primary remanent magnetization (PRM; solid black) is acquired. (b) Southward tilting of ~5° of E_{1d} between ~62 and 54 Ma, remagnetization induced by paleoweathering happened, and a chemical remanent magnetization (CRM₁; dashed gray) carried by secondary hematite was acquired. E_{2n} was deposited subsequently at ~62–54 Ma. (c) Continued southward tilting of E_{1d} and E_{2n} to ~15° before eruption of E_{2p} volcanic rocks. Subsequently, E_{2p} was erupted/deposited, and massive dykes (pink) intruded E_{1d} and E_{2n} at ~54–48 Ma at ~20°N latitude. Strong remagnetizations were induced due to thermochemical and thermoviscous overprinting. Hematite formed during the high-temperature hydrothermal alteration and a second CRM (CRM₂; dashed gray) was acquired. Combination of CRM₁ and CRM₂ results in a remanent magnetization (solid red) carried by hematite with low inclination. Part of Ti-poor titanomagnetite acquired a thermoviscous remanent magnetization (TVRM₁; dashed gray). A combination of PRM and TVRM₁ resulted in a remanent magnetization (solid blue) carried by Ti-poor titanomagnetite with low inclination. PRM carried by Ti-rich titanomagnetite is completely reset to TVRM₁. (d) Northward tilting of ~30° of the entire sequence between 48 and 13 Ma. (e) Remanent magnetization carried by Ti-rich titanomagnetite was erased again after tilting and a new TVRM (TVRM₂; dashed purple) was acquired at ~20°N latitude at ~13 Ma related to Miocene dykes (green) intruded into E_{1d} . Note that E_{1d} and E_{2n} are ~270 and ~330 m thick, respectively, whereas the volcanic rocks in E_{2p} have a thickness of ~1900 m [He *et al.*, 2007].

Given that our results show that E_{1d} volcanic rocks in the Linzhou basin have been remagnetized, we conclude that the results from E_{1d} volcanic rocks reported by *Chen et al.* [2010] and *Chen et al.* [2014] are also likely to be remagnetized and therefore cannot be used for paleolatitude calculations. Our results preclude the large and rapid Late Cretaceous to early Paleogene latitude oscillation of the Lhasa terrane inferred by *Chen et al.* [2014]. Instead, the conclusions presented here are consistent with recent reviews of robust paleomagnetic data from Cretaceous and younger volcanic rocks and other inclination shallowing-corrected sedimentary rocks from the Lhasa terrane that demonstrate relatively stable paleolatitudes of Lhasa terrane from ~110 to 50 Ma [van Hinsbergen *et al.*, 2012; Lippert *et al.*, 2014]. Our results are also consistent with the predictions from the Eurasian apparent polar wander path that suggest no significant paleolatitudinal motions for stable Eurasia occurred during Late Cretaceous to early Cenozoic times [Torsvik *et al.*, 2012], and

the finding that not more than 600–750 km of intra-Asian shortening has occurred during the Cenozoic [Dewey *et al.*, 1989; Lippert *et al.*, 2011; van Hinsbergen *et al.*, 2011b].

We conclude that the NRM carried by Ti-rich titanomagnetite in the dykes and E_{1d} lavas of the lower Linzizong volcanic rocks in the Linzhou basin was overprinted by later thermal resetting. We also have shown that lavas and sedimentary rocks of the lower Linzizong Group have been variably remagnetized by low-temperature fluid flow and precipitation of secondary hematite in the Nanmulin basin [Huang *et al.*, 2015b] and by high-temperature fluid alteration and thermal resetting in the Linzhou basin. Our work on the remagnetized lower Linzizong volcanic rocks in the Linzhou basin also highlights that hematite in volcanic rocks should be suspected of carrying a secondary, and sometimes misinterpreted, remanent magnetization. We implore future paleomagnetic studies in this region to be vigilant in appraising the remanence carriers and thus inferring primary magnetizations. Our work underscores the utility of acquiring thorough rock magnetic, petrographic, and geochronologic information in tectonically directed paleomagnetic research. Paleomagnetic studies that have characterized paleosecular variation, assessed datasets for sedimentary inclination shallowing, and tested for remagnetization yield a consistent Paleogene latitude of $\sim 20 \pm 4^\circ\text{N}$ for the Lhasa terrane. This paleolatitude indicates that the collision between the Tibetan Himalaya and the Lhasa terrane began by ~ 52 Ma, if not earlier [Dupont-Nivet *et al.*, 2010b; Najman *et al.*, 2010; van Hinsbergen *et al.*, 2012; DeCelles *et al.*, 2014; Garzanti and Hu, 2014; Hu *et al.*, 2014; Lippert *et al.*, 2014].

10. Conclusions

Paleomagnetic studies of the Paleogene Linzizong Group in the Linzhou basin by several independent teams have yielded a range of paleolatitude estimates for the Lhasa terrane from $\sim 20^\circ\text{N}$ from the volcanic rocks in upper intervals (E_{2p}) to $\sim 5^\circ\text{N}$ from the volcanic rocks in the lower intervals (E_{1d}) [Chen *et al.*, 2010; Dupont-Nivet *et al.*, 2010b; Tan *et al.*, 2010; Chen *et al.*, 2014]. Here we have reevaluated this section by thorough sampling of the volcanic rocks from both the lower and upper intervals to test the reproducibility of the previous results and to assess why different intervals yield such different paleolatitude estimates within a short window of geologic time. We completed comprehensive paleomagnetic analyses, microscopic investigations, and geochronologic studies, which lead us to conclude the following:

1. The paleomagnetic directions of Chen *et al.* [2010] and Chen *et al.* [2014] from E_{1d} lavas are reproducible.
2. Magnetic carriers for E_{1d} are magmatic titanomagnetite and secondary hematite, whereas magnetic carriers for E_{2p} are dominated by magmatic titanomagnetite with negligible amounts of secondary hematite.
3. Whole rock $^{40}\text{Ar}/^{39}\text{Ar}$ ages of lavas from E_{1d} are ~ 10 Myr younger than zircon U-Pb ages, suggesting a post-emplacment thermal disturbance. In contrast, whole rock $^{40}\text{Ar}/^{39}\text{Ar}$ ages of lavas from E_{2p} are consistent with zircon U-Pb ages.
4. Volcanic rocks from E_{1d} are probably remagnetized due to acquisition of secondary chemical remanent magnetization carried by post-emplacment hematite and thermoviscous remanent magnetization carried by titanomagnetite.
5. Volcanic rocks from E_{1d} cannot be used to determine the Paleogene paleolatitude of the Lhasa terrane. All available evidence, however, suggest that the Paleogene paleolatitude of the Lhasa terrane of $\sim 20 \pm 4^\circ\text{N}$ determined from volcanic rocks from E_{2p} is reliable. Our results reported here, as well as those published elsewhere, suggest that the Tibetan Himalaya-Lhasa collision was underway by or slightly before 52 Ma.
6. In addition to a secondary origin of hematite as cause for the remagnetization, we also detect the acquisition of secondary thermoviscous remanent magnetization in the volcanic rocks from the lower Linzizong Group. Future paleomagnetic studies in tectonically active regions should be vigilant in assessing sampled units for hydrothermal fluid activity with related thermal anomalies.

References

- Aben, F. M., M. J. Dekkers, R. R. Bakker, D. J. J. van Hinsbergen, W. J. Zachariasse, G. W. Tate, N. McQuarrie, R. Harris, and B. Duffy (2014), Untangling inconsistent magnetic polarity records through an integrated rock magnetic analysis: A case study on Miocene sections in East Timor, *Geochem. Geophys. Geosyst.*, *15*, 2531–2554, doi:10.1002/2014GC005294.
- Achache, J., V. Courtillot, and Z. Y. Xiu (1984), Paleogeographic and tectonic evolution of southern Tibet since middle Cretaceous time: New paleomagnetic data and synthesis, *J. Geophys. Res.*, *89*(B12), 10,311–10,339, doi:10.1029/JB089iB12p10311.
- Allegre, C. J., V. Courtillot, P. Tapponnier, A. Hirn, and M. Mattauer (1984), Structure and evolution of the Himalaya-Tibet orogenic belt, *Nature*, *307*, 17–22.

Acknowledgments

Data to support this article are available in Tables S1–S8 in the supporting information. This work was funded by the U.S. NSF Continental Dynamics grant EAR-1008527 “The Suturing Process: Insight from the India-Asia Collision Zone,” the Netherlands Organization for Scientific Research (NWO) with VIDI grants to GD-N (864.08.005) and DJJvH (864.11.004), the China Scholarship Council to WH, the ERC Starting Grant 306810 (SINK) to DJJvH, the Alexander von Humboldt foundation to GD-N, and the Cai Yuanpei program of the French Ministries of Foreign Affairs and of higher education and research and the Chinese Ministry Of Education. We thank Maxim Krasnoperov for lab assistance, and Liao Chang and Cor G. Langereis for discussions. We are grateful to Kenneth P. Kodama, John W. Geissman, and the Associate Editor for their constructive comments and suggestions.

- Anson, G., and K. Kodama (1987), Compaction-induced inclination shallowing of the post-depositional remanent magnetization in a synthetic sediment, *Geophys. J. Int.*, *88*(3), 673–692.
- Appel, E., R. Müller, and R. Widder (1991), Paleomagnetic results from the Tibetan Sedimentary Series of the Manang area (north central Nepal), *Geophys. J. Int.*, *104*(2), 255–266.
- Appel, E., A. Patzelt, and C. Chouker (1995), Secondary paleoremanence of Tethyan sediments from the Zaskar Range (NW Himalaya), *Geophys. J. Int.*, *122*(1), 227–242.
- Biggin, A. J., D. J. van Hinsbergen, C. G. Langereis, G. B. Straathof, and M. H. Deenen (2008), Geomagnetic secular variation in the Cretaceous Normal Superchron and in the Jurassic, *Phys. Earth Planet. Inter.*, *169*(1), 3–19.
- Borradaile, G., D. W. Davis, R. Middleton, and I. Geneviciene (2008), Remagnetization (~1100 Ma) of Voosges lake tuff (1542 Ma) and other mid-proterozoic rocks, Nipigon graben, northern Ontario, *Precambrian Res.*, *161*(3), 341–354.
- Bureau of Geology and Mineral Resources of Xizang Autonomous Region (BGMRXAR) (1993), *Regional Geology of Xizang (Tibet) Autonomous Region*, *Geol. Mem. Ser.*, vol. 1, 707 pp., Geological House, Beijing.
- Burg, J. P., and G. M. Chen (1984), Tectonics and structural zonation of southern Tibet, China, *Nature*, *311*, 219–223.
- Burg, J. P., F. Proust, P. Tapponnier, and G. M. Chen (1983), Deformation phases and tectonic evolution of the Lhasa block (southern Tibet, China), *Eclogae Geol. Helv.*, *76*(3), 643–665.
- Callot, J. P., and L. Geoffroy (2004), Magma flow in the East Greenland dyke swarm inferred from study of anisotropy of magnetic susceptibility: Magmatic growth of a volcanic margin, *Geophys. J. Int.*, *159*(2), 816–830.
- Callot, J.-P., L. Geoffroy, C. Aubourg, J. Pozzi, and D. Mege (2001), Magma flow directions of shallow dykes from the East Greenland volcanic margin inferred from magnetic fabric studies, *Tectonophysics*, *335*(3), 313–329.
- Chen, J., B. Huang, and L. Sun (2010), New constraints to the onset of the India-Asia collision: Paleomagnetic reconnaissance on the Linzizong Group in the Lhasa Block, China, *Tectonophysics*, *489*(1–4), 189–209.
- Chen, J., B. Huang, Z. Yi, L. Yang, and L. Chen (2014), Paleomagnetic and $^{40}\text{Ar}/^{39}\text{Ar}$ geochronologic results from the Linzizong Group, Linzhou Basin, Lhasa Terrane, Tibet: Implications to Paleogene paleolatitude and onset of the India-Asia collision, *J. Asian Earth Sci.*, *96*, 162–177.
- Chen, W., T. Yang, S. Zhang, Z. Yang, H. Li, H. Wu, J. Zhang, Y. Ma, and F. Cai (2012), Paleomagnetic results from the Early Cretaceous Zenong Group volcanic rocks, Cuoqin, Tibet, and their paleogeographic implications, *Gondwana Res.*, *22*(2), 461–469.
- Chen, Y., and V. Courtillot (1989), Widespread Cenozoic (?) remagnetization in Thailand and its implications for the India-Asia collision, *Earth Planet. Sci. Lett.*, *93*(1), 113–122.
- Chen, Y., V. Courtillot, J.-P. Cogne, J. Besse, Z. Yang, and R. Enkin (1993), The configuration of Asia prior to the collision of India: Cretaceous paleomagnetic constraints, *J. Geophys. Res.*, *98*(B12), 21,927–21,941, doi:10.1029/93JB02075.
- Coulon, C., H. Maluski, C. Bollinger, and S. Wang (1986), Mesozoic and Cenozoic volcanic rocks from central and southern Tibet: ^{39}Ar - ^{40}Ar dating, petrological characteristics and geodynamical significance, *Earth Planet. Sci. Lett.*, *79*(3–4), 281–302.
- Craig, J. R. (2001), Ore-mineral textures and the tales they tell, *Can. Mineral.*, *39*(4), 937–956.
- Day, R., M. Fuller, and V. Schmidt (1977), Hysteresis properties of titanomagnetites: Grain-size and compositional dependence, *Phys. Earth Planet. Inter.*, *13*(4), 260–267.
- de Sigoyer, J., V. R. Chavagnac, J. Blichert-Toft, I. M. Villa, B. A. Luais, S. P. Guillot, M. Cosca, and G. Mascle (2000), Dating the Indian continental subduction and collisional thickening in the northwest Himalaya: Multichronology of the Tso Moriri eclogites, *Geology*, *28*(6), 487–490.
- de Wall, H., S. Schöbel, M. K. Pandit, K. K. Sharma, and J. Just (2010), A record of ductile syn-intrusional fabrics to post solidification cataclasis: Magnetic fabric analysis of neoproterozoic Mirpur and Mt., Abu Granitoids, NW India, *J. Geol. Soc. India*, *75*(1), 239–253.
- Deamer, G. A., and K. P. Kodama (1990), Compaction-induced inclination shallowing in synthetic and natural clay-rich sediments, *J. Geophys. Res.*, *95*(B4), 4511–4529, doi:10.1029/JB4095iB4504p04511.
- DeCelles, P., P. Kapp, G. Gehrels, and L. Ding (2014), Paleocene-Eocene foreland basin evolution in the Himalaya of southern Tibet and Nepal: Implications for the age of initial India-Asia collision, *Tectonics*, *33*, 824–849, doi:10.1002/2014TC003522.
- Deenen, M. H. L., C. G. Langereis, D. J. J. van Hinsbergen, and A. J. Biggin (2011), Geomagnetic secular variation and the statistics of paleomagnetic directions, *Geophys. J. Int.*, *186*(2), 509–520.
- Dekkers, M. J. (2012), End-member modelling as an aid to diagnose remagnetization: A brief review, *Geol. Soc. London Spec. Publ.*, *371*(1), 253–269.
- Dewey, J. F., R. M. Shackleton, C. Chengfa, and S. Yiyin (1988), The tectonic evolution of the Tibetan Plateau, *R. Soc. London*, *327*, 379–413.
- Dewey, J., S. Cande, and W. C. Pitman (1989), Tectonic evolution of the India/Eurasia collision zone, *Eclogae Geol. Helv.*, *82*(3), 717–734.
- Ding, L., P. Kapp, D. Zhong, and W. Deng (2003), Cenozoic volcanism in Tibet: Evidence for a transition from oceanic to continental subduction, *J. Petrol.*, *44*(10), 1833–1865.
- Ding, L., Q. Xu, Y. Yue, H. Wang, F. Cai, and S. Li (2014), The Andean-type Gangdese Mountains: Paleoelevation record from the Paleocene-Eocene Linzhou Basin, *Earth Planet. Sci. Lett.*, *392*, 250–264.
- Dunlop, D. J., and Ö. Özdemir (1997), *Rock Magnetism: Fundamentals and Frontiers*, 573 pp., Cambridge Univ. Press, Cambridge, U. K.
- Dunlop, D. J., P. W. Schmidt, Ö. Özdemir, and D. A. Clark (1997), Paleomagnetism and paleothermometry of the Sydney Basin 1. Thermoviscous and chemical overprinting of the Milton Monzonite, *J. Geophys. Res.*, *102*(B12), 27,271–27,283, doi:10.1029/27297JB02479.
- Dunlop, D. J., Ö. Özdemir, D. Clark, and P. Schmidt (2000), Time-temperature relations for the remagnetization of pyrrhotite (Fe_7S_8) and their use in estimating paleotemperatures, *Earth Planet. Sci. Lett.*, *176*(1), 107–116.
- Dupont-Nivet, G., D. J. J. van Hinsbergen, and T. H. Torsvik (2010a), Persistently low Asian paleolatitudes: Implications for the India-Asia collision history, *Tectonics*, *29*, TC5016, doi:10.1029/2008TC002437.
- Dupont-Nivet, G., P. C. Lippert, D. J. J. van Hinsbergen, M. J. M. Meijers, and P. Kapp (2010b), Palaeolatitude and age of the Indo-Asia collision: Palaeomagnetic constraints, *Geophys. J. Int.*, *182*(3), 1189–1198.
- Edel, J. B., and T. Aifa (2001), Paleomagnetic evolution of the Armorican Massif in Late Paleozoic times, in the light of overprints recorded in Cadomian and Paleozoic units, *Tectonophysics*, *331*(1), 145–167.
- Edel, J., and J. Schneider (1995), The Late Carboniferous to Early Triassic geodynamic evolution of Variscan Europe in the light of magnetic overprints in Early Permian rhyolites from the northern Vosges (France) and central Black Forest (Germany), *Geophys. J. Int.*, *122*(3), 858–876.
- Egli, R. (2004), Characterization of individual rock magnetic components by analysis of remanence curves, 1. Unmixing natural sediments, *Stud. Geophys. Geod.*, *48*(2), 391–446.
- Elmore, R. D., D. London, D. Bagley, D. Fruit, and G. Gao (1993), Remagnetization by basinal fluids: Testing the hypothesis in the Viola Limestone, southern Oklahoma, *J. Geophys. Res.*, *98*(B4), 6237–6254, doi:10.1029/6292JB02577.
- Elmore, R. D., A. R. Muxworthy, and M. Aldana (2012), Remagnetization and chemical alteration of sedimentary rocks, *Geol. Soc. London Spec. Publ.*, *371*(1), 1–21.
- Enkin, R. J., K. G. Osadetz, J. Baker, and D. Kisilevsky (2000), Orogenic remagnetizations in the Front Ranges and Inner Foothills of the southern Canadian Cordillera: Chemical harbinger and thermal handmaiden of Cordilleran deformation, *Geol. Soc. Am. Bull.*, *112*(6), 929–942.

- Evans, D., N. Beukes, and J. Kirschvink (2002), Paleomagnetism of a lateritic paleoweathering horizon and overlying Paleoproterozoic red beds from South Africa: Implications for the Kaapvaal apparent polar wander path and a confirmation of atmospheric oxygen enrichment, *J. Geophys. Res.*, *107*(B12), 2326, doi:10.1029/2001JB000432.
- Fisher, R. A. (1953), Dispersion on a sphere, *Proc. R. Soc. London, Ser. A*, *217*, 295–305.
- Font, E., R. Trindade, and A. Nédélec (2006), Remagnetization in bituminous limestones of the Neoproterozoic Araras Group (Amazon craton): Hydrocarbon maturation, burial diagenesis, or both?, *J. Geophys. Res.*, *111*, B06204, doi:10.1029/2005JB004106.
- Font, E., A. Rapalini, R. Tomezzoli, R. Trindade, and E. Tohver (2012), Episodic remagnetizations related to tectonic events and their consequences for the South America Polar Wander Path, *Geol. Soc. London Spec. Publ.*, *371*(1), 55–87.
- Garzanti, E., and X. Hu (2014), Latest Cretaceous Himalayan tectonics: Obduction, Collision Or Deccan-related uplift?, *Gondwana Res.*, doi:10.1016/j.gr.2014.1003.1010.
- Garzanti, E., A. Baud, and G. Mascle (1987), Sedimentary record of the northward flight of India and its collision with Eurasia (Ladakh Himalaya, India), *Geodin Acta*, *1*(4/5), 297–312.
- Geissman, J. W., and S. S. Harlan (2002), Late Paleozoic remagnetization of Precambrian crystalline rocks along the Precambrian/Carboniferous nonconformity, Rocky Mountains: A relationship among deformation, remagnetization, and fluid migration, *Earth Planet. Sci. Lett.*, *203*(3), 905–924.
- Gilder, S., and V. Courtillot (1997), Timing of the North-South China collision from new middle to late Mesozoic paleomagnetic data from the North China Block, *J. Geophys. Res.*, *102*(B8), 17,713–17,727, doi:10.1029/17797JB01201.
- Gong, Z., D. van Hinsbergen, and M. Dekkers (2009a), Diachronous pervasive remagnetization in northern Iberian basins during Cretaceous rotation and extension, *Earth Planet. Sci. Lett.*, *284*(3), 292–301.
- Gong, Z., M. Dekkers, D. Heslop, and T. Mullender (2009b), End-member modelling of isothermal remanent magnetization (IRM) acquisition curves: A novel approach to diagnose remagnetization, *Geophys. J. Int.*, *178*(2), 693–701.
- Gradstein, F. M., J. G. Ogg, M. Schmitz, and G. Ogg (2012), *The Geologic Time Scale 2012*, Cambridge Univ. Press, Cambridge, U. K.
- Green, O. R., M. P. Searle, R. I. Corfield, and R. M. Corfield (2008), Cretaceous-Tertiary Carbonate Platform Evolution and the Age of the India-Asia Collision along the Ladakh Himalaya (Northwest India), *J. Geol.*, *116*(4), 331–353, doi:10.1086/588831.
- Guillot, S., G. Mahéo, J. De Sigoyer, K. H. Hattori, and A. Pêcher (2008), Tethyan and Indian subduction viewed from the Himalayan high- to ultrahigh-pressure metamorphic rocks, *Tectonophysics*, *451*(1), 225–241.
- Hargraves, R., D. Johnson, and C. Chan (1991), Distribution anisotropy: The cause of AMS in igneous rocks?, *Geophys. Res. Lett.*, *18*(12), 2193–2196, doi:10.1029/2191GL01777.
- Harlan, S. S., J. W. Geissman, L. W. Snee, and R. L. Reynolds (1996), Late Cretaceous remagnetization of Proterozoic mafic dykes, southern Highland Mountains, southwestern Montana: A paleomagnetic and $^{40}\text{Ar}/^{39}\text{Ar}$ study, *Geol. Soc. Am. Bull.*, *108*(6), 653–668.
- Harrison, R. J., and J. M. Feinberg (2008), FORCinel: An improved algorithm for calculating first-order reversal curve distributions using locally weighted regression smoothing, *Geochem. Geophys. Geosyst.*, *9*, Q05016, doi:10.1029/2008GC001987.
- He, S., P. Kapp, P. G. DeCelles, G. E. Gehrels, and M. Heizler (2007), Cretaceous-Tertiary geology of the Gangdese Arc in the Linzhou area, southern Tibet, *Tectonophysics*, *433*(1–4), 15–37.
- Heslop, D., G. McIntosh, and M. J. Dekkers (2004), Using time- and temperature-dependent Preisach models to investigate the limitations of modelling isothermal remanent magnetization acquisition curves with cumulative log Gaussian functions, *Geophys. J. Int.*, *157*(1), 55–63.
- Hu, X., H. D. Sinclair, J. Wang, H. Jiang, and F. Wu (2012), Late Cretaceous-Paleogene stratigraphic and basin evolution in the Zhepure Mountain of southern Tibet: Implications for the timing of India-Asia initial collision, *Basin Res.*, *24*(5), 520–543.
- Hu, X., W. An, J. Wang, E. Garzanti, and R. Guo (2014), Himalayan detrital chromian spinels and timing of Indus-Yarlung ophiolite erosion, *Tectonophysics*, *621*, 60–68.
- Huang, W., G. Dupont-Nivet, P. C. Lippert, D. J. van Hinsbergen, and E. Hallot (2013), Inclination shallowing in Eocene Linzizong sedimentary rocks from Southern Tibet: Correction, possible causes and implications for reconstructing the India-Asia collision, *Geophys. J. Int.*, *194*(3), 1390–1411.
- Huang, W., D. J. J. Van Hinsbergen, M. Maffione, D. A. Orme, G. Dupont-Nivet, C. Guilmette, L. Ding, Z. Guo, and P. Kapp (2015a), Lower Cretaceous Xigaze ophiolite formed in the Gangdese forearc: Evidence from paleomagnetism, sediment provenance, and stratigraphy, *Earth Planet. Sci. Lett.*, doi:10.1016/j.epsl.2015.1001.1032.
- Huang, W., et al. (2015b), Can a primary remanence be retrieved from partially remagnetized Eocene volcanics in the Nanmulin Basin (Southern Tibet) to date the India-Asia collision?, *J. Geophys. Res. Solid Earth*, *120*, 42–66, doi:10.1002/2014JB011599.
- Huang, W., et al. (2015c), Paleolatitudes of the Tibetan Himalaya from primary and secondary magnetizations of Jurassic to Lower Cretaceous sedimentary rocks, *Geochem. Geophys. Geosyst.*, *16*, 77–100, doi:10.1002/2014GC005624.
- Jackson, M. J., J. A. Banerjee, R. L. Marvin, and W. Grueber (1991), Detrital remanence inclination errors, and anhysteretic remanence anisotropy: Quantitative model and experimental results, *Geophys. J. Int.*, *104*, 95–103.
- Jackson, M., and N. L. Swanson-Hysell (2012), Rock magnetism of remagnetized carbonate rocks: Another look, *Geol. Soc. London Spec. Publ.*, *371*(1), 229–251.
- Jelinek, V. (1981), Characterization of the magnetic fabric of rocks, *Tectonophysics*, *79*, T63–T67.
- Jiang, Z., et al. (2014), Transition from oceanic to continental lithosphere subduction in southern Tibet: Evidence from the Late Cretaceous-Early Oligocene (~91–30 Ma) intrusive rocks in the Chanang-Zedong area, southern Gangdese, *Lithos*, *196–197*, 213–231.
- Johnson, C. L., et al. (2008), Recent investigations of the 0–5 Ma geomagnetic field recorded by lava flows, *Geochem. Geophys. Geosyst.*, *9*, Q04032, doi:10.1029/2007GC001696.
- Johnson, M. R. W. (2002), Shortening budgets and the role of continental subduction during the India-Asia collision, *Earth Sci. Rev.*, *59*(1–4), 101–123.
- Just, J., A. Kontry, H. De Wall, A. M. Hirt, and F. Martín-Hernández (2004), Development of magnetic fabrics during hydrothermal alteration in the Soutz-sous-Forets granite from the EPS-1 borehole, Upper Rhine Graben, *Geol. Soc. London Spec. Publ.*, *238*(1), 509–526.
- Kapp, P., P. G. DeCelles, G. E. Gehrels, M. Heizler, and L. Ding (2007a), Geological records of the Lhasa-Qiangtang and Indo-Asian collisions in the Nima area of central Tibet, *Geol. Soc. Am. Bull.*, *119*(7–8), 917–933.
- Kapp, P., P. G. DeCelles, A. L. Leier, J. M. Fabijanic, S. He, A. Pullen, G. E. Gehrels, and L. Ding (2007b), The Gangdese retroarc thrust belt revealed, *GSA Today*, *17*(7), 4–9.
- Kent, D. V. (1985), Thermoviscous remagnetization in some Appalachian limestones, *Geophys. Res. Lett.*, *12*(12), 805–808, doi:10.1029/GL1012i1012p00805.
- Kent, D. V., and J. D. Miller (1987), Redbeds and thermoviscous magnetization theory, *Geophys. Res. Lett.*, *14*(4), 327–330, doi:10.1029/GL014i004p00327.
- King, R. F. (1955), The remanent magnetism of artificially deposited sediments, *Geophys. J. Int.*, *7*, 115–134.
- Kirschvink, J. (1980), The least-squares line and plane and the analysis of palaeomagnetic data, *Geophys. J. Int.*, *62*(3), 699–718.
- Kodama, K. P. (2012), *Paleomagnetism of Sedimentary Rocks: Process and Interpretation*, 157 pp., Wiley-Blackwell, Chichester, U. K.

- Kruiver, P. P., and H. F. Passier (2001), Coercivity analysis of magnetic phases in sapropel S1 related to variations in redox conditions, including an investigation of the S-ratio, *Geochim. Geophys. Geosyst.*, 2(12), 1063, doi:10.1029/2001GC000181.
- Kruiver, P. P., M. J. Dekkers, and D. Heslop (2001), Quantification of magnetic coercivity components by the analysis of acquisition curves of isothermal remanent magnetisation, *Earth Planet. Sci. Lett.*, 189(3), 269–276.
- Kumar, A. (1986), Palaeolatitudes and the age of Indian laterites, *Palaeogeogr. Palaeoclimatol. Palaeoecol.*, 53(2), 231–237.
- Kumar, A., and M. Bhalla (1984), Palaeomagnetism of Sukinda chromites and their geological implications, *Geophys. J. Int.*, 77(3), 863–874.
- Lee, H. Y., S.-L. Chung, Y. Wang, D. Zhu, J. Yang, B. Song, D. Liu, and F. Wu (2007), Age, petrogenesis and geological significance of the Linzizong volcanic successions in the Linzhou basin, southern Tibet: Evidence from zircon U-Pb dates and Hf isotopes, *Acta Petrol. Sin.*, 23(2), 493–500.
- Lee, H. Y., S. L. Chung, C. H. Lo, J. Ji, T. Y. Lee, Q. Qian, and Q. Zhang (2009), Eocene Neotethyan slab breakoff in southern Tibet inferred from the Linzizong volcanic record, *Tectonophysics*, 477(1–2), 20–35.
- Leech, M. L., S. Singh, A. K. Jain, S. L. Klemperer, and R. M. Manickavasagam (2005), The onset of India-Asia continental collision: Early, steep subduction required by the timing of UHP metamorphism in the western Himalaya, *Earth Planet. Sci. Lett.*, 234, 83–97.
- Leier, A. L., P. G. DeCelles, P. Kapp, and L. Ding (2007), The Takena Formation of the Lhasa terrane, southern Tibet: The record of a Late Cretaceous retroarc foreland basin, *Geol. Soc. Am. Bull.*, 119(1–2), 31–48.
- Liebke, U., E. Appel, L. Ding, U. Neumann, B. Antolin, and Q. Xu (2010), Position of the Lhasa terrane prior to India-Asia collision derived from paleomagnetic inclinations of 53 Ma old dykes of the Linzhou Basin: Constraints on the age of collision and post-collisional shortening within the Tibetan Plateau, *Geophys. J. Int.*, 182(3), 1199–1215.
- Liebke, U., E. Appel, U. Neumann, and L. Ding (2012), Dual polarity directions in basaltic-andesitic dykes-reversal record or self-reversed magnetization?, *Geophys. J. Int.*, 190(2), 887–899.
- Lin, J., and D. R. Watts (1988), Paleomagnetic constrains on Himalayan-Tibetan tectonic evolution, *Philos. Trans. R. Soc. London*, 326, 177–188.
- Lippert, P. C., X. X. Zhao, R. S. Coe, and C. H. Lo (2011), Palaeomagnetism and $^{40}\text{Ar}/^{39}\text{Ar}$ geochronology of upper Palaeogene volcanic rocks from Central Tibet: Implications for the Central Asia inclination anomaly, the palaeolatitude of Tibet and post-50 Ma shortening within Asia, *Geophys. J. Int.*, 184(1), 131–161.
- Lippert, P. C., D. J. J. van Hinsbergen, and G. Dupont-Nivet (2014), The Early Cretaceous to Present latitude of the central Lhasa-plano (Tibet): A paleomagnetic synthesis with implications for Cenozoic tectonics, paleogeography and climate of Asia, in *Towards an Improved Understanding of Uplift Mechanisms and the Elevation History of the Tibetan Plateau*, *Geol. Soc. Am. Spec. Pap.*, vol. 507, edited by J. S. Nie, G. D. Hoke, and B. K. Horton, pp. 1–21, Geol. Soc. of Am., Boulder, Colo.
- Liu, C., K. Ge, C. Zhang, Q. Liu, C. Deng, and R. Zhu (2011), Nature of remagnetization of Lower Triassic red beds in southwestern China, *Geophys. J. Int.*, 187(3), 1237–1249.
- Liu, H. (1993), Classification and age attribution of the Linzizong volcanic series in the Lhasa area of Tibet [in Chinese], *Tibetan Geol.*, 10(2), 59–68.
- Løvlie, R., and T. Torsvik (1984), Magnetic remanence and fabric properties of laboratory-deposited hematite-bearing red sandstone, *Geophys. Res. Lett.*, 11(3), 221–224, doi:10.1029/GL1011i1003p00221.
- Lowrie, W. (1990), Identification of ferromagnetic minerals in a rock by coercivity and unblocking temperature properties, *Geophys. Res. Lett.*, 17(2), 159–162, doi:10.1029/GL1017i1002p00159.
- Ma, Y., T. Yang, Z. Yang, S. Zhang, H. Wu, H. Li, H. Li, W. Chen, J. Zhang, and J. Ding (2014), Paleomagnetism and U-Pb zircon geochronology of Lower Cretaceous lava flows from the western Lhasa terrane: New constraints on the India-Asia collision process and intracontinental deformation within Asia, *J. Geophys. Res. Solid Earth*, 119, 7404–7424, doi:10.1002/2014JB011362.
- MacDonadl, W., and H. Palmer (1990), Flow directions in ash-flow tuffs: A comparison of geological and magnetic susceptibility measurements, Tshirege member (upper Bandelier Tuff), Valles caldera, New Mexico, USA, *Bull. Volcanol.*, 53(1), 45–59.
- McCabe, C., R. Van der Voo, D. R. Peacor, C. R. Scotese, and R. Freeman (1983), Diagenetic magnetite carries ancient yet secondary remanence in some Paleozoic sedimentary carbonates, *Geology*, 11(4), 221–223.
- McDougall, I., and T. M. Harrison (1999), *Geochronology and Thermochronology by the $^{40}\text{Ar}/^{39}\text{Ar}$ Method*, Oxford Univ. Press, Oxford, U. K.
- McFadden, P. L., and F. J. Lowes (1981), The discrimination of mean directions drawn from Fisher distributions, *Geophys. J. R. Astronomical Soc.*, 67, 19–33.
- Meijers, M. J. M., D. J. J. van Hinsbergen, M. J. Dekkers, D. Altner, N. Kaymakci, and C. G. Langereis (2011), Pervasive Paleogene remagnetization of the central Taurides fold-and-thrust belt (southern Turkey) and implications for rotations in the Sparta Angle, *Geophys. J. Int.*, 184(3), 1090–1112.
- Middleton, M. F., and P. W. Schmidt (1982), Paleothermometry of the Sydney basin, *J. Geophys. Res.*, 87(B7), 5351–5359, doi:10.1029/JB5087iB5307p05351.
- Miller, J. D., and D. V. Kent (1988), Regional trends in the timing of Alleghanian remagnetization in the Appalachians, *Geology*, 16(7), 588–591.
- Mo, X., Z. Zhao, J. Deng, G. C. Dong, S. Zhou, T. Y. Guo, S. Q. Zhang, and L. L. Wang (2003), Response of volcanism to the India-Asia collision, *Earth Sci. Front.*, 10(3), 135–148.
- Mo, X., Z. Hou, Y. Niu, G. Dong, X. Qu, Z. Zhao, and Z. Yang (2007), Mantle contributions to crustal thickening during continental collision: Evidence from Cenozoic igneous rocks in southern Tibet, *Lithos*, 96(1), 225–242.
- Molina Garza, R. S. M., and J. D. A. Zijderveld (1996), Paleomagnetism of Paleozoic strata, Brabant and Ardennes Massifs, Belgium: Implications of pre-folding and post-folding Late Carboniferous secondary magnetizations for European apparent polar wander, *J. Geophys. Res.*, 101(B7), 15,799–15,818, doi:10.1029/15796JB00325.
- Mullender, T. A. T., T. Frederichs, C. Hilgenfeldt, K. Fabian, and M. J. Dekkers (2005), Fully automated demagnetization and measurement of NRM, ARM and IRM on a '2G' SQUID magnetometer, *IAGA*, Abstract IAGA2005-A-00898.
- Najman, Y., E. Appel, M. Boudagher-Fadel, P. Bown, A. Carter, E. Garzanti, L. Godin, J. Han, U. Liebke, and G. Oliver (2010), Timing of India-Asia collision: Geological, biostratigraphic, and palaeomagnetic constraints, *J. Geophys. Res.*, 115, B12416, doi:10.1029/2010JB007673.
- Néel, L. (1949), Théorie du trainage magnétique des ferromagnétiques en grains fins avec applications aux terres cuites, *Ann. Geophys.*, 5(2), 99–136.
- Orme, D. A., B. Carrapa, and P. Kapp (2014), Sedimentology, provenance and geochronology of the upper Cretaceous-lower Eocene western Xigaze forearc basin, southern Tibet, *Basin Res.*, 1–25, doi:10.1111/bre.12080.
- Otofujii, Y.-I., K. Takemoto, H. Zaman, Y. Nishimitsu, and Y. Wada (2003), Cenozoic remagnetization of the Paleozoic rocks in the Kitakami massif of northeast Japan, and its tectonic implications, *Earth Planet. Sci. Lett.*, 210(1), 203–217.
- Pan, F.-B., H.-F. Zhang, W.-C. Xu, L. Guo, S. Wang, and B.-j. Luo (2014), U-Pb zircon chronology, geochemical and Sr-Nd isotopic composition of Mesozoic-Cenozoic granitoids in the SE Lhasa terrane: Petrogenesis and tectonic implications, *Lithos*, 192–195(0), 142–157.

- Parcerisa, D., C. Franke, C. Fabrega, K. Yao, and M. Thiry (2013), Implications from paleomagnetic age constraints and petrology analyses on the reconstruction of the Triassic paleosurface in Europe—Examples from Catalonia and the Polish Sudetes, paper presented at AGU Fall Meeting 2013.
- Pike, C. R., A. P. Roberts, and K. L. Verosub (1999), Characterizing interactions in fine magnetic particle systems using first order reversal curves, *J. Appl. Phys.*, *85*(9), 6660–6667.
- Pozzi, J.-P., M. Westphal, Y. X. Zhou, L. S. Xing, and X. Y. Chen (1982), Position of the Lhasa block, South Tibet, during the late Cretaceous, *Nature*, *297*, 319–321.
- Preeden, U., S. Mertenan, T. Elminen, and J. Plado (2009), Secondary magnetizations in shear and fault zones in southern Finland, *Tectonophysics*, *479*(3), 203–213.
- Pulliaiah, G., E. Irving, K. L. Buchan, and D. J. Dunlop (1975), Magnetization changes caused by burial and uplift, *Earth Planet. Sci. Lett.*, *28*(2), 133–143.
- Rapalini, A. E., and L. S. Bettucci (2008), Widespread remagnetization of late Proterozoic sedimentary units of Uruguay and the apparent polar wander path for the Rio de La Plata craton, *Geophys. J. Int.*, *174*(1), 55–74.
- Renne, P. R., C. C. Swisher, A. L. Deino, D. B. Karner, T. L. Owens, and D. J. DePaolo (1998), Intercalibration of standards, absolute ages and uncertainties in $^{40}\text{Ar}/^{39}\text{Ar}$ dating, *Chem. Geol.*, *145*(1), 117–152.
- Replumaz, A., and P. Tapponnier (2003), Reconstruction of the deformed collision zone between India and Asia by backward motion of lithospheric blocks, *J. Geophys. Res.*, *108*(B6), 2285, doi:10.1029/2001JB000661.
- Ricordel, C., D. Parcerisa, M. Thiry, M. G. Moreau, and D. Gómez-Gras (2007), Triassic magnetic overprints related to albitization in granites from the Morvan massif (France), *Palaeogeogr. Palaeoclimatol. Palaeoecol.*, *251*(2), 268–282.
- Roberts, A. P., Y. Cui, and K. L. Verosub (1995), Wasp-waisted hysteresis loops: Mineral magnetic characteristics and discrimination of components in mixed magnetic systems, *J. Geophys. Res.*, *100*(B9), 17,909–17,924, doi:10.1029/17995JB00672.
- Roberts, A. P., C. R. Pike, and K. L. Verosub (2000), First-order reversal curve diagrams: A new tool for characterizing the magnetic properties of natural samples, *J. Geophys. Res.*, *105*(28), 28,461–28,475, doi:10.1029/22000JB900326.
- Roberts, A. P., F. Florindo, J. C. Larrasoana, M. A. O'Regan, and X. Zhao (2010), Complex polarity pattern at the former Plio-Pleistocene global stratotype section at Vrica (Italy): Remagnetization by magnetic iron sulphides, *Earth Planet. Sci. Lett.*, *292*(1), 98–111.
- Rochette, P., C. Aubourg, and M. Perrin (1999), Is this magnetic fabric normal? A review and case studies in volcanic formations, *Tectonophysics*, *307*(1), 219–234.
- Schmidt, P., D. Currey, and C. Ollier (1976), Sub-basaltic weathering, damsites, palaeomagnetism, and the age of lateritization, *J. Geol. Soc. Aust.*, *23*(4), 367–370.
- Schöbel, S., and H. de Wall (2014), AMS–NRM interferences in the Deccan basalts: Towards an improved understanding of magnetic fabrics in flood basalts, *J. Geophys. Res. Solid Earth*, *119*, 2651–2678, doi:10.1002/2013JB010660.
- Sengor, A. M. C. (1984), The Cimmeride orogenic system and the tectonics of Eurasia, *Geol. Soc. Am. Spec. Pap.*, *195*, 82.
- Smith, R. T., and K. L. Verosub (1994), Thermoviscous remanent magnetism of Columbia River Basalt blocks in the Cascade landslide, *Geophys. Res. Lett.*, *21*(24), 2661–2664, doi:10.1029/2694GL02669.
- Sun, Z., W. Jiang, H. Li, J. Pei, and Z. Zhu (2010), New paleomagnetic results of Paleocene volcanic rocks from the Lhasa block: Tectonic implications for the collision of India and Asia, *Tectonophysics*, *490*(3), 257–266.
- Sun, Z., J. Pei, H. Li, W. Xu, W. Jiang, Z. Zhu, X. Wang, and Z. Yang (2012), Palaeomagnetism of late Cretaceous sediments from southern Tibet: Evidence for the consistent palaeolatitudes of the southern margin of Eurasia prior to the collision with India, *Gondwana Res.*, *21*(1), 53–63.
- Tan, X., S. Gilder, K. P. Kodama, W. Jiang, Y. Han, H. Zhang, H. Xu, and D. Zhou (2010), New paleomagnetic results from the Lhasa block: Revised estimation of latitudinal shortening across Tibet and implications for dating the India-Asia collision, *Earth Planet. Sci. Lett.*, *293*(3), 396–404.
- Tapponnier, P., M. Mattauer, F. Proust, and C. Cassaigneau (1981), Mesozoic ophiolites, sutures, and large-scale tectonic movements in Afghanistan, *Earth Planet. Sci. Lett.*, *52*, 355–371.
- Tauxe, L., and D. V. Kent (2004), A simplified statistical model for the geomagnetic field and the detection of shallow bias in paleomagnetic inclinations: Was the ancient magnetic field dipolar, *Timescales Paleomagnetic Field*, *145*, 101–115.
- Tauxe, L., T. Mullender, and T. Pick (1996), Potbellies, wasp-waists, and superparamagnetism in magnetic hysteresis, *J. Geophys. Res.*, *101*(B1), 571–583, doi:10.1029/1095JB03041.
- Tauxe, L., K. P. Kodama, and D. V. Kent (2008), Testing corrections for paleomagnetic inclination error in sedimentary rocks: A comparative approach, *Phys. Earth Planet. Int.*, *169*(1–4), 152–165.
- Team of Regional Geological Survey of the Bureau of Geology and Mineral Resources of Tibet Autonomous Region (1990), *Regional Geological Map of Tibet, Scale 1:500,000*, Geological House, Beijing.
- Théveniaut, H., and P. Freyssinet (2002), Timing of lateritization on the Guiana Shield: Synthesis of paleomagnetic results from French Guiana and Suriname, *Palaeogeogr. Palaeoclimatol. Palaeoecol.*, *178*(1), 91–117.
- Torsvik, T. H., and L. R. M. Cocks (2013), Gondwana from top to base in space and time, *Gondwana Res.*, *24*(3), 999–1030.
- Torsvik, T. H., R. D. Müller, R. Van der Voo, B. Steinberger, and C. Gaina (2008), Global plate motion frames: Toward a unified model, *Rev. Geophys.*, *46*, RG3004, doi:10.1029/2007RG000227.
- Torsvik, T. H., R. Van der Voo, U. Preeden, C. Mac Niocaill, B. Steinberger, P. V. Doubrovine, D. J. J. van Hinsbergen, M. Domeier, C. Gaina, and E. Tohver (2012), Phanerozoic polar wander, palaeogeography and dynamics, *Earth Sci. Rev.*, *114*(3), 325–368.
- Turner, M. B., S. J. Cronin, R. B. Stewart, M. Bebbington, and I. E. Smith (2008), Using titanomagnetite textures to elucidate volcanic eruption histories, *Geology*, *36*(1), 31–34.
- Valet, J. P., T. Kidane, V. Soler, J. Brassart, V. Courtillot, and L. Meynadier (1998), Remagnetization in lava flows recording pretransitional directions, *J. Geophys. Res.*, *103*(B5), 9755–9775, doi:10.1029/9797JB03544.
- van der Voo, R., and T. H. Torsvik (2012), The history of remagnetization of sedimentary rocks: Deceptions, developments and discoveries, *Geol. Soc. London Spec. Publ.*, *371*(1), 23–53.
- Van Hinsbergen, D. J. J., M. J. Dekkers, and A. Koc (2010), Testing Miocene remagnetization of Bey Dağları: Timing and amount of Miocene rotations in SW Turkey, *Turkish J. Earth Sci.*, *19*, 123–156.
- van Hinsbergen, D. J. J., B. Steinberger, P. V. Doubrovine, and R. Gassmöller (2011a), Acceleration and deceleration of India-Asia convergence since the Cretaceous: Roles of mantle plumes and continental collision, *J. Geophys. Res.*, *116*, B06101, doi:10.1029/2010JB008051.
- van Hinsbergen, D. J. J., P. Kapp, G. Dupont-Nivet, P. C. Lippert, P. G. Decelles, and T. H. Torsvik (2011b), Restoration of Cenozoic deformation in Asia and the size of Greater India, *Tectonics*, *30*, TC5003, doi:10.1029/2011TC002908.
- van Hinsbergen, D. J. J., P. C. Lippert, G. Dupont-Nivet, N. McQuarrie, P. V. Doubrovine, W. Spakman, and T. H. Torsvik (2012), Greater India Basin hypothesis and a two-stage Cenozoic collision between India and Asia, *Proc. Natl. Acad. Sci. U.S.A.*, *109*(20), 7659–7664.

- Weil, A. B., and R. Van der Voo (2002), Insights into the mechanism for orogen-related carbonate remagnetization from growth of authigenic Fe-oxide: A scanning electron microscopy and rock magnetic study of Devonian carbonates from northern Spain, *J. Geophys. Res.*, *107*(B4), 2063, doi:10.1029/2001JB000200.
- Weltje, G. J. (1997), End-member modeling of compositional data: Numerical-statistical algorithms for solving the explicit mixing problem, *Math. Geol.*, *29*(4), 503–549.
- Westphal, M., and J.-P. Pozzi (1983), Paleomagnetic and plate tectonic constraints on the movement of Tibet, *Tectonophysics*, *98*(1–2), 1–10.
- Wu, X., Y. Feng, and J. Huang (2005), Geochemical characteristics of Nianbo Formation at Cuoqin County, Tibet and its geotectonic significance, *J. East China Inst. Technol.*, *28*(1), 1–9.
- Xu, R. H., U. Scharer, and C. J. Allegre (1985), Magmatism and metamorphism in the Lhasa block (Tibet): A geochronologic study, *J. Geol.*, *93*(1), 41–57.
- Yang, T., Y. Ma, S. Zhang, W. Bian, Z. Yang, H. Wu, H. Li, W. Chen, and J. Ding (2014), New insights into the India-Asia collision process from Cretaceous paleomagnetic and geochronologic results in the Lhasa terrane, *Gondwana Res.*, doi:10.1016/j.gr.2014.1006.1010.
- Yin, A., and M. T. Harrison (2000), Geologic evolution of the Himalayan-Tibetan orogen, *Annu. Rev. Earth Planet. Sci.*, *28*, 211–280.
- Yue, Y., and L. Ding (2006), $^{40}\text{Ar}/^{39}\text{Ar}$ Geochronology, geochemical characteristics and genesis of the Linzhou basic dykes, Tibet, *Acta Petrol. Sin.*, *22*(4), 855–866.
- Yuquans, Z. (1995), Thermal evolution of the Gangdese batholith, southern Tibet: A history of episodic unroofing, *Tectonics*, *14*(2), 223–236, doi:10.1029/1094TC01676.
- Zhou, S., X. Mo, G. Dong, Z. Zhao, R. Qiu, T. Guo, and L. Wang (2004), $^{40}\text{Ar}/^{39}\text{Ar}$ geochronology of Cenozoic Linzizong volcanic rocks from Linzhou Basin, Tibet, China, and their geological implications, *Chin. Sci. Bull.*, *49*(18), 1970–1979.
- Zhu, Z., X. Zhu, and Y. Zhang (1981), Paleomagnetic observation in Xizang (Tibet) and continental drift, *Acta Geophys. Sin.*, *24*(2), 40–49.